



# Geochemical signatures of potassium metasomatism in anthracite from the Himalayan fold-thrust belts of Sikkim, India

Santanu Ghosh<sup>1,2</sup> · Anwita Ojha<sup>1</sup> · Atul Kumar Varma<sup>1</sup>

Received: 20 August 2021 / Accepted: 2 April 2022  
© The Author(s) 2022

## Abstract

The present study focuses on the inorganic geochemical features of the bituminous coal samples from the Raniganj and the Jharia Basins, as well as the anthracite samples from the Himalayan fold-thrust belts of Sikkim, India. The SiO<sub>2</sub> content (48.05 wt% to 65.09 wt% and 35.92 wt% to 50.11 wt% in the bituminous and anthracite samples, respectively) and the ratio of Al<sub>2</sub>O<sub>3</sub>/TiO<sub>2</sub> (6.97 to 17.03 in the bituminous coal samples and 10.34 to 20.07 in the anthracite samples) reveal the intermediate igneous source rock composition of the minerals. The ratio of the K<sub>2</sub>O/Al<sub>2</sub>O<sub>3</sub> in the ash yield of the bituminous coal samples (0.03 to 0.09) may suggest the presence of kaolinite mixed with montmorillonite, while its range in the ash yield of the anthracite samples (0.16 to 0.27) may imply the presence of illite mixed with kaolinite. The chemical index of alteration values may suggest the moderate to strong chemical weathering of the source rock under sub-humid to humid climatic conditions. The plot of the bituminous coal samples in the A–CN–K diagram depicts the traditional weathering trend of parent rocks, but the anthracite samples plot near the illite field and are a bit offset from the weathering trend. This may imply the plausible influences of the potassium-metasomatism at post coalification stages, which is further supported by high K<sub>2</sub>O/Na<sub>2</sub>O ratio (29.88–80.13). The Fourier transform infrared spectra further reveal the hydroxyl stretching intensity of illite in the anthracite samples substantiating the effect of the epigenetic potassium-metasomatism. The decrease in total kaolinite intensity/compound intensity of quartz and feldspar may provide additional evidence towards this epigenetic event.

**Keywords** Himalayan fold-thrust belts · Anthracite · Potassium metasomatism · Kaolinite to quartz-feldspar intensity ratio · Montmorillonite stretching and bending intensities · Illite-stretching frequency

## 1 Introduction

The nature and the abundances of the minerals in coals may influence their utilization in industries (Dai et al. 2018; Finkelman 1994; Finkelman et al. 2019; Gupta et al. 1999; Raask 1985; Ward 1984, 2002; Zhao et al. 2013). Accurate knowledge of the mineral matter in the coal is necessary to avoid ash deposition in boilers, emission of volatiles during coal combustion (Dai et al. 2018) as well as to reduce abrasion, corrosion, stickiness associated with coal processing

(Finkelman 1994; Ward 2002, 2016). Minerals, especially the clay minerals having swelling property may reduce roof stability (Mark and Molinda 2005; Kang et al. 2015; Li et al. 2016) and may also lead to frictional ignition of methane during mining operations (Finkelman et al. 2019). Clay minerals also create handling issues during preparation and transport of coals (French 2018). The presence of minerals with low melting temperature may result in bed agglomeration and collapse of the fluidized bed in fluidized bed combustors, which may in turn lead to the shutdown of the boiler (French 2018). Minerals can also affect the microstructural organization of coals as depicted by the microwave irradiation technique (Yang et al. 2021). Additionally, the minerals may adversely influence the coal gasification (Liu et al. 2019), and even the presence of minerals with low melting point may lead to the ash handling problems, which may in turn result in the shutdown of the gasifier (French 2018). Moreover, the pyrite and apatite in coals may deliver large amounts of sulfur and phosphorus, and therefore alleviate

✉ Atul Kumar Varma  
atul@iitism.ac.in

<sup>1</sup> Coal Geology and Organic Petrology Laboratory, Department of Applied Geology, Indian Institute of Technology (Indian School of Mines), Dhanbad, Jharkhand 826004, India

<sup>2</sup> Department of Earth Sciences, Indian Institute of Technology Bombay, Powai, Mumbai, Maharashtra 400076, India

the caking ability, while the conversion of quartz to cristobalite weakens and ruptures the coke (Finkelman et al. 2019). Besides, the minerals and the toxic elements hosted by them may impart deleterious effects on human health and environment (Dai et al. 2008, 2021; Huang et al. 2006; Large et al. 2009; Tian 2005; Tian et al. 2008 among others).

Although having so much detrimental effects, the minerals in coals are also beneficial in many aspects. Iron sulfides catalyse the liquefaction procedure, while smectite clay may impart beneficial cracking influence on the coal liquefaction products (Finkelman et al. 2019). Pyrite may enhance the hydrocarbon potential from kerogen through the catalytic activity of sulfur (Larsen and Hu 2006; Ma et al. 2016). Further, iron-bearing clay mineral, like nontronite can enhance the bioavailability of coal by generating strongly-oxidizing hydroxyl radicals, which may assist in enhanced microbial recovery of the coal bed methane (Hu et al. 2021). Further, the bulk coal and the ash are the sources of rare earth elements (REEs) and Y, Ga, Li, Zr, Nb, and Se (Bullock et al. 2018; Dai and Finkelman 2018; Lin et al. 2018; Seredin and Finkelman 2008; Zhao et al. 2018), which are in the utmost demand in the semiconductor industries (Finkelman et al. 2019). In complementary, the mineral matter in the coal can act as graphitization catalyst for coal char, turbostratic carbon, coal tar pitch matrix, etc. (González et al. 2005; Oya and Marsh 1982; Rodrigues et al. 2012; Wang et al. 2001). Kaolinite and illite are observed as the potential catalysts for carbonaceous materials (Bonijoly et al. 1982; Marsh and Warburton 1970; Oberlin and Terriere 1975; Oya and Marsh 1982; Rodrigues et al. 2012; Wang et al. 2001, 2021), and in the presence of iron (González et al. 2005; Oya and Marsh 1982), they can improve the degree of structural ordering of the carbonaceous materials during high-temperature treatment.

The X-ray fluorescence (XRF), and Fourier transform infrared (FTIR) spectroscopy, among many other methods, document the inorganic geochemical characteristics of organic-rich source rocks efficiently. The major elemental oxides obtained from the XRF data reveal the parent rock composition and intensity of chemical weathering of those parent rocks (Bai et al. 2015; Fedo et al. 1995; Hazra et al. 2016; Moradi et al. 2016; Nesbitt and Young 1982; Tao et al. 2017; Varma et al. 2018; Zhang et al. 2018) as well as the palaeotectonic setting (Roser and Korsch 1986). The XRF data also discriminates the input of feldspar and clays through the ratio of potassium oxide to alumina ( $K_2O/Al_2O_3$ ) as well as from the index of compositional variation (ICV) (Cox et al. 1995) in the organic-rich rocks. The FTIR data reveals the absorbance intensities of mineral matter like kaolinite, quartz, feldspar, siderite, etc. (Hazra et al. 2016; Varma et al. 2018) present in the organic-rich source rocks.

In this study, the inorganic geochemical characteristics of the bituminous coal samples from the Raniganj and the

Jharia Basin as well as that of the anthracite samples from the Sikkim Himalayan fold-thrust belts of India have been studied employing the XRF, and the FTIR techniques. Coals of anthracite rank (more specifically, anthracite A rank; ISO 11760 (2005)) are best preserved within the Ranig-tectonic window at the complex fold-thrust belts of the Sikkim Himalayas (Ghosh 1997; Ghosh et al. 2018a; GSI 2012). These coals were reported to be intensely affected by the deformation episodes of the Himalayan orogeny and consequent metamorphism (Ghosh 1997; GSI 2012). They revealed unique optical (more specifically, microstructural properties) and organic geochemical features, which were reported for the first time by Anwita et al. (2020) and Ghosh et al. (2018a, 2020). These unique features of these anthracite samples were compared with those of the bituminous coal samples from the Raniganj and the Jharia Basins, the two most productive basins for coal and coal bed methane. Those comparisons revealed enthralling transformations of the microstructural and organic geochemical characteristics of organic matter with the coal metamorphism (or advent in the coal rank) from the bituminous stage to anthracite rank (Anwita et al. 2020; Ghosh et al. 2020). So, these basins (Raniganj and Jharia) and the Sikkim Himalayan fold-thrust belts turned out to be geologically fascinating to study the responses of the organic matter to the geological events. Previously, a lot of investigations focused on the microstructural, organic geochemical and hydrocarbon generation perspectives of the bituminous coals and shale samples from the Raniganj and the Jharia Basins (Anwita et al. 2020; Ghosh et al. 2018b, 2020; Hazra et al. 2015, 2018a, 2018b, 2018c; Misra et al. 2018, 2019; Singh et al. 2021; Tiwari et al. 2020; Varma et al. 2014 among others). Meanwhile, any inorganic geochemical transformations with increasing coal rank were barely investigated from these areas hitherto. This research question forms the basis of the present investigation whether the minerals in these coals responded to the coal metamorphism or to the geological events. Further, there was an urge to study the plausible response of the clay minerals within the Sikkim anthracite samples to the Himalayan deformation and metamorphic events. To quench these quests, the clay mineral facets of the bituminous coals from the Raniganj and the Jharia Basins, which are relatively tectonically least disturbed and less metamorphosed, are compared with the clay mineralogical framework of the tectonically disturbed and highly metamorphosed anthracite samples from the Sikkim Himalayan fold-thrust belts.

The objectives of the present study are to manifest the clay mineralogy from the ash yield of the bituminous and the anthracite coal samples, as well as to document any plausible secondary alteration of the clay mineral framework of the anthracite samples during metamorphism. The novelty of this investigation lies in the proposition of the epigenetic potassium metasomatism (K-metasomatism) in

the anthracite samples for the first time and the discussions of the influences of this metasomatic event on the clay mineralogical framework of these samples. To point out the influences of K-metasomatism on the clay mineralogy of the anthracite samples in a more precise way, they have also compared these samples with the ash yield of some selected bituminous coal samples, which are found not to experience this event. The authors have supported that comparison with the FTIR spectroscopy, which was barely reported hitherto. Additionally, the total intensities of kaolinite ( $TI_K$ ) and quartz along with feldspar ( $TI_{Q-F}$ ) from the FTIR spectra are introduced in this investigation for the first time to support the influences of the K-metasomatism on the clay mineralogy of the anthracite samples. This also contributes to the novelty of this research. Further, the authors have introduced a new index, namely the palaeohumidity factor (PHF), to determine the paleoclimatic condition during the source rock weathering episodes through modifying the 'C-value' proposed by Zhao et al. (2007). The knowledge of the clay mineralogy of the studied bituminous coal samples can be employed for their better utilization in the industries. On the other hand, the information on the clay mineral framework of the anthracite samples may help in understanding the catalytic effects of these minerals for synthetic graphite production.

## 2 Geological setting

The tentative locations of the sampling sites are furnished in the map of India (Fig. 1). The geological details of the study area are elaborated as follows:

### 2.1 Raniganj Basin

The Raniganj Basin (Fig. 2; following Gee 1932), a significant part of the Damodar Valley Basin, is situated between  $23^{\circ} 22' N$ – $23^{\circ} 52' N$ ;  $86^{\circ} 36' E$ – $87^{\circ} 30' E$  and encompasses an aerial extent of  $1900 \text{ km}^2$ . This basin was initially a sag basin that later formed a homoclinal geometry with the deposition of the Talchir and the Barakar sediments (Gee 1932). The meandering rivers on the north side of this basin supplied the organic matter, whereas, in the eastern part, the peat mires were developed with fanlomeratic cones (Ghosh 2002). The west-bound rivers in this basin contributed the organic detritus along with clastic sediments to deposit peats in the western part of this basin (Ghosh 2002). Table 1 presents the general stratigraphy of the Raniganj Basin (following GSI 2003; Mukhopadhyay et al. 2010). As two of the studied bituminous coal samples were collected from the Barakar and the Raniganj Formation of the Raniganj Basin, brief discussions of those two formations are mentioned below.

#### 2.1.1 Barakar Formation

The Barakar Formation comprises white to fawn-colored sandstone carbonaceous shale, fire-clays, and coal beds reflecting a braided to fluvio-lacustrine alluvial deposit. The lower and the middle units of this formation comprise a thicker coal seam than the upper unit. The Barakar Formation is the principal coal-bearing unit in the Lower Gondwana formations. The coal seams intercalate with the sandstone and shale beds. This formation is thicker in the northern and the western parts of this basin, while it becomes thinner towards the east and south. It has a maximum thickness of 750 m.

#### 2.1.2 Raniganj Formation

The Raniganj Formation consists of a large number of regionally developed coal seams of commercial importance. The Raniganj Formation is characterized by a sequence of sandstone-shale-coal sequence in which different lithology exhibits broad fining upward cycles. The sandstones in this formation are fine-grained and of uniform character compared to that in the Barakar Formation. The sandstones are associated with micaceous siltstone, sandy shales, dark grey shales, and coal seams. The Raniganj Formation attains a maximum thickness of 1150 m at the Surajnagar area located south-east of Asansol in the western part of the Raniganj Basin (GSI 2003).

### 2.2 Jharia Basin

Jharia Basin (Fig. 3; following Fox 1930; Mishra and Cook 1992) comprises a large reserve of bituminous coking coals that can be used in the metallurgical industries (Mishra and Cook 1992). This basin extends between  $23^{\circ} 37' N$ – $23^{\circ} 52' N$  and  $86^{\circ} 06' E$ – $86^{\circ} 30' E$  with a total area of  $456 \text{ km}^2$ , and this basin forms a half-graben structure (Basu and Shrivastava 1981; Mishra and Cook 1992). The basinal axis has a plunge towards the west with an east–west trend. Meanwhile, the southern boundary fault had deformed the southern flank of this basin with a throw of around 1500 m (GSI 1977; Mishra and Cook 1992; Verma 1983). The stratigraphic successions of this basin are depicted in Table 2 (following Chandra 1992; Fox 1930, GSI 1977). The bituminous coal samples were collected from the Barakar and the Raniganj Formation of the Jharia Basin. Short discussions of these two formations are manifested below.

#### 2.2.1 Barakar Formation

The Barakar Formation comprises fluvial sediments, and this is the most important coal-bearing formation consisting of coarse-grained sandstones, conglomerates, siltstones,



**Fig. 1** Study areas with samples (tentative locations) in the map of India (following Ghosh et al. 2020)

fireclays, carbonaceous shales, and coal seams. The coal seams in this formation are thick and may indicate the slow sinking of this basin.

### 2.2.2 Raniganj Formation

The Raniganj Formation is exposed in an oval basin with an areal extent of 58 square kilometers and has a maximum thickness of 800 m (Chandra 1992). This formation is the uppermost coal-bearing unit in the Jharia Basin. The Raniganj Formation consists of coarse- to fine-grained sandstones, shales, carbonaceous shales, and coal seams. Fox (1930) had recognized three regional coal seams in Mohuda, Bhurungiya, and Pathargaria and eight local seams in the

Raniganj Formation. Sengupta (1980) had identified thirteen coal seams and numbered them from 0 to XII. The No. 0 seam corresponds to the Mohuda Bottom seam, and the No. XII (XIIA and XIIB) is assigned to the Telmucha seams.

### 2.3 Sikkim Himalayan fold-thrust belts

Sikkim state extending from 27° 05' N to 28° 08' N and 88° 10' E to 88° 55' E is bordered by the southern ranges of the Eastern Himalayan Mountain belts with 7096 km<sup>2</sup> area (GSI 2012). The tectonic compressional stress had deformed the preceding thrust systems and developed the Himalayan fold-thrust belts (Valdiya 1980; Gansser 1964; Ray 1995; Bhattacharyya and Mitra 2009). The Teesta and Rangit

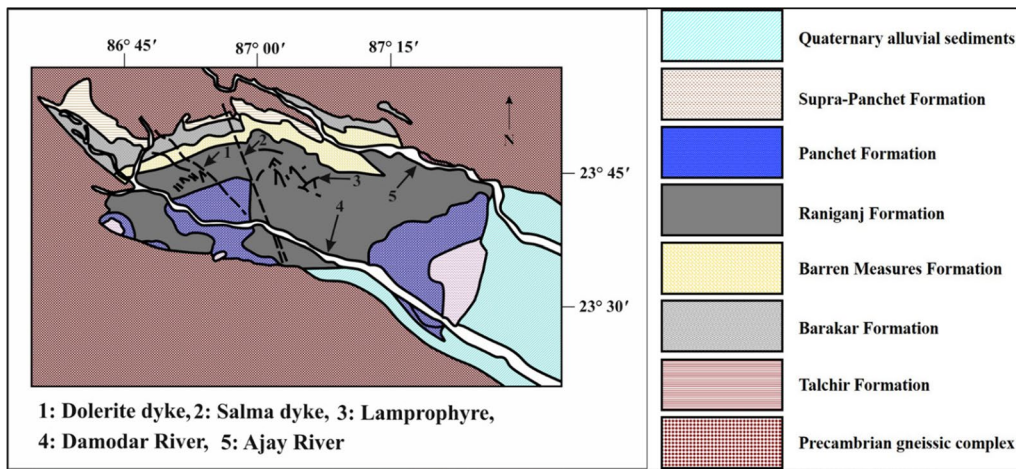
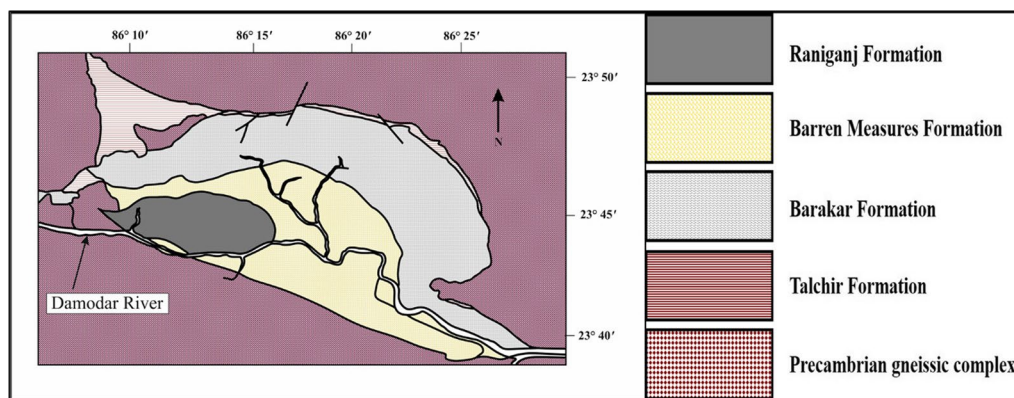


Fig. 2 Map of the Raniganj Basin, India (following Gee 1932)

Table 1 Stratigraphic successions of the Raniganj Basin (following GSI 2003; Mukhopadhyay et al. 2010)

Age	Formation	Lithology	Thickness (m)
Recent and quaternary		Alluvial and residual soils; lateritic capping	90
Tertiary		Light grey mudstone and siltstone with bands of marlstone; white, soft fine grained clayey sandstone, mottled clay and loose sand with pebbles of vein quartz; occasionally lignite at the basal part	300
Cretaceous	Igneous intrusives	Basic (dolerite) dykes; Ultrabasic (mica-peridotite, mica-lamprophyre, lamprophyre) sills and dykes	–
Cretaceous	Rajmahal Formation	Greenish grey to black, fine to medium grained vesicular porphyritic basalt and volcanic breccia; weathered aphanitic basalt at places; one to five inter-trappeans consisting of grey shale, fine grained sandstone and carbonaceous shales	120
Upper Triassic	Supra-Panchet	Massive, very coarse to coarse quartzose sandstone, conglomeratic at places; bands of dark red silty shale	300
Lower Triassic	Panchet	Coarse grained greenish yellow and greenish grey soft, micaceous, cross-bedded sandstone with slump structures; khaki green fissile silty shale; alternate bands of yellow coarse grained immature sandstone and bright reddish-brown claystone with calcareous concretions; conglomeratic at the base	600
Upper Permian	Raniganj	Grey to light grey fine and medium grained micaceous feldspathic sandstone with calcareous clayey matrix in the upper part; siltstones and shales, often interlaminated with fine grained sandstone; carbonaceous shales and coal beds	1150
	Barren measures	Dark grey to black micaceous or carbonaceous, fissile shales with ferruginous laminae and thin bands of dense, hard, cryptocrystalline clay ironstones; rarely interbanded with fine-grained sandstone	600
Lower Permian	Barakar Formation with Kaharbari Formation (?) at base	Very coarse to medium grained arkosic sandstones, often cross-bedded; grey and carbonaceous shales, at times interbanded with fine grained sandstone; fire clay lenses and coal beds; pebbly and carbonaceous in lower part	750
	Talchir	Tillite or diamictite with sandy or clayey matrix at the base; medium to fine grained khaki or yellowish green feldspathic sandstone; siltstone, silty shale, needle shale and rhythmite with dropstones	500
Precambrian	Chotanagpur Gneissic Complex	Granite gneiss with migmatitic gneiss, hornblende schist, hornblende gneiss, metabasic rocks, pegmatite and quartz veins etc	–





**Fig. 3** Map of the Jharia Basin, India (following Fox 1930; Mishra and Cook 1992)

**Table 2** Stratigraphic successions of the Jharia Basin (following Chandra 1992; Fox 1930; GSI 1977)

Age	Epoch	Formation	Lithology	Thickness (m)
Jurassic or Tertiary			Dolerite dykes	–
Lower Jurassic			Mica lamprophyre dykes and sills	–
Upper Permian	Lopingian (260 to 252.2 Ma)	Raniganj	Fine-grained feldspathic sandstone, shales with coal seams	800
Middle Permian	Gaudalupian (271 to 260 Ma)	Barren Measures	Buff colored sandstones shales and carbonaceous shales	730
Lower Permian	Cisularianan (299 to 271 Ma)	Barakar	Buff colored coarse and medium- grained feldspathic sandstones, grits, shales, carbonaceous shales and coal seams	1250
		Talchir	Greenish shale and fine-grained sandstones	245
Precambrian			Metamorphic rocks	–

rivers acted as the erosion agent in this area and shaped the ‘Teesta half window’ (Schwan 1980). The ‘Lesser Himalayan Sequence’ uncovers greenschist facies metamorphic rocks at this half window (Bhattacharyya and Mitra 2011). Buxa and Daling lithology, along with the Gondwana sequences, exhibited multiple repetitions in this sequence, a portion of which is exposed as the Rangit duplex at the Rangit window (Fig. 4; following Bhattacharyya and Mitra 2009) lying within the Teesta half window (Bhattacharyya et al. 2006). The intense tectonism had influenced the microstructural characteristics of the Gondwana lithology and enhanced the rank of the coal to the anthracite A (Ghosh et al. 2018a). The general stratigraphic layout within the Sikkim Himalayan fold-thrust belts (following GSI 2012) is shown in Table 3. A brief of the Damuda Formation, from which the coal samples were collected is demonstrated below.

### 2.3.1 Damuda Formation

The Damuda Formation shows prominent exposure in the Rangit Window and outcrops on Naya Bazar–Legship road section, Jorethang–Namchi road section, and adjoining areas.

The Damuda Formation comprises sandstone, calcareous sandstone, shale, carbonaceous shale, and coal seams. The sandstones are intercalated with carbonaceous slate, fissile black slate, and in places with coal seams. The coal seams had lost a lot of volatile matter and turned into anthracite rank. The coal deposits exhibit pinching and swelling structures. They are found almost in the pulverized state due to brittle failure of the grains originated from intense tectonism of the Himalayas (GSI 2012). They have also shown evidence of thermo-stress coupling on their microstructure driven by the Himalayan orogeny (Ghosh et al. 2018a, 2020).

## 3 Materials and methods

### 3.1 Sampling

A total of fifteen (15) coal samples were collected from the Raniganj and the Jharia Basins as well as from the Sikkim Himalayan fold-thrust belts (FTBs) of India to carry out this study (Table 4). A total of eight (8) coals from these basins were collected through channel sampling procedure, following the guidelines mentioned in ISO 14180 (2017).

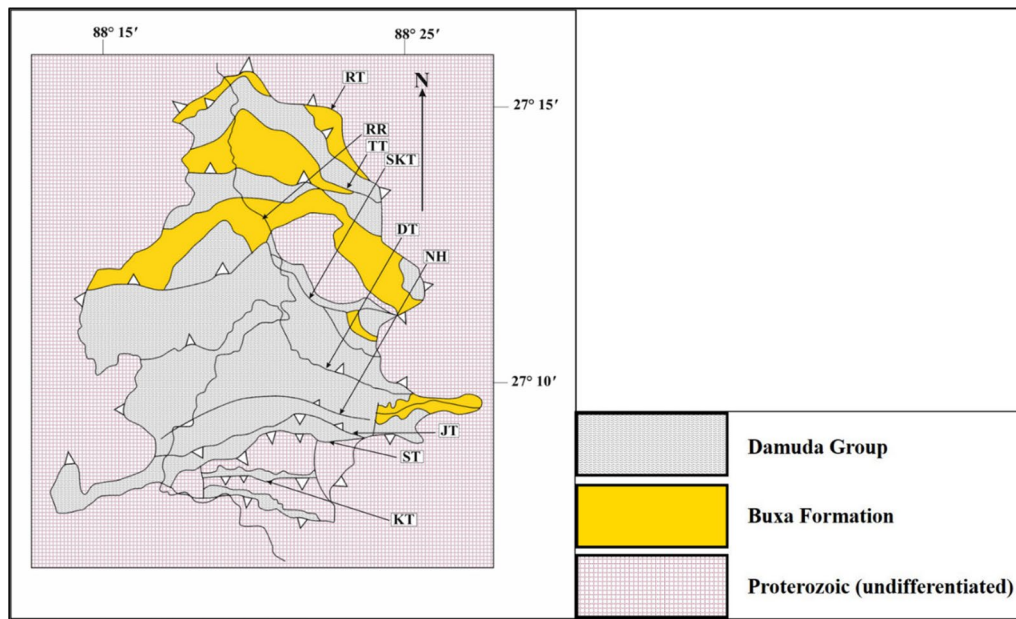


**Fig. 4** Map of the Rangit window, Sikkim Himalayan fold-thrust belts of India (following Bhattacharyya and Mitra 2009). *Notes:* RT refers to Ramgarh Thrust; TT refers to Tatapani Thrust; SKT refers

to Sikkip Thrust; DT refers to Dong Thrust; JT refers to Jorethang Thrust; ST refers to Sorok Thrust; KT refers to Kitam Thrust; NH refers to Namchi Horse; RR refers to Rangit River

**Table 3** Stratigraphic successions of the Himalayan fold-thrust belts (following GSI 2012)

Age	Group/formation	Lithology
Upper Pleistocene-Holocene	Sesela Formation	Variegated clay, fine and medium-grained sand, pebble bed
	Intrusive	Tourmaline/biotite leuco-granite, schroll rock/pegmatite, apatite (undifferentiated)
Triassic	Tso Lahmo Formation	Fossiliferous sandstone, limestone, shale
Carboniferous-Permian	Lachi Formation	Boulder bed, fossiliferous sandstone, limestone, shale
	Damuda Group	Sandstone, shale, carboniferous shale and coal
Ordovician	Rangit pebble slate Groups	Pebble/boulder slate, conglomerate, phyllite
	Everest Limestone Formation	Fossiliferous limestone with quartzite
	Lingste Granite Gneiss	Phyllite, quartzite, biotite gneiss
	Sill	Amphibolite
	Buxa Formation	Dolostone, ortho-quartzite, chert, purple phyllite
Proterozoic (undifferentiated)	Reyang Formation	Ortho-quartzite, pyritiferous black slate, meta-greywacke, variegated chert, phyllite
	Daling Group/Gorubathan Formation	Interbanded chlorite-sericite schist, phyllite, quartzite, meta-greywacke, pyritiferous black slate, biotite schist, quartzite
	Kanchenjunga Gneiss/Darjeeling Gneiss (undifferentiated)	Migmatite, augen (garnet) biotite gneiss, sillimanite with palaeosomes of staurolite, kyanite, mica schist, sillimanite gneiss, granite gneiss
	Chungthang Formation	Quartzite, garnet-kyanite-sillimanite-biotite schist, calc-silicates

CG1671 and CG1672 samples belong to the Raniganj and the Barakar Formations of the Raniganj Basin, respectively. CG1674 belongs to the Raniganj Formation of the Jharia Basin, while CG1673 and CG1675–CG1679 samples were collected from the Barakar Formation of the Jharia Basin (Anwita et al. 2020; Ghosh et al. 2020). Besides, a total of seven (7) coal samples were collected from road cut

sections, which traverse through Jorethang-Namchi-Nayabazar-Legship-Sikkip-Reshi towns of the west and south Sikkim (Table 4). CG3300, CG3301, and CG3302 samples were picked up from the Jorethang area and CG3303 was collected near Namchi at the south Sikkim. Sample CG3304 was sampled from the north of the Kamling village (Ghosh et al. 2018a, 2020). Furthermore, CG3305 and

**Table 4** Sampling sites of coals from the Raniganj and the Jharia Basins as well as from Himalayan fold-thrust belts of Sikkim, India (following Ghosh et al. 2020)

Sample No.	Name of colliery	Seam No.	Formation/group	Basin/area	State
CG1671	Satgram	Rotibati-G4, Ghusik A seam	Raniganj Formation	Raniganj Basin	West Bengal
CG1672	Satgram	Kuardih, Seam No. 14	Barakar Formation	Raniganj Basin	West Bengal
CG1673	Brindabanpur	BP seam (top section)	Barakar Formation	Jharia Basin	Jharkhand
CG1674	Barari	VII bottom seam	Raniganj Formation	Jharia Basin	Jharkhand
CG1675	Maheshpur	IX top seam	Barakar Formation	Jharia Basin	Jharkhand
CG1676	Lohapatti	XIV seam	Barakar Formation	Jharia Basin	Jharkhand
CG1677	Damagoria	Salaspur 'C' seam	Barakar Formation	Jharia Basin	Jharkhand
CG1679	Dahibari-Basantimata	Gopinathpur bottom seam	Barakar Formation	Jharia Basin	Jharkhand
CG3300	–	–	Damuda Group	Jorethang	Sikkim
CG3301	–	–	Damuda Group	Jorethang	Sikkim
CG3302	–	–	Damuda Group	Jorethang	Sikkim
CG3303	–	–	Damuda Group	Namchi	Sikkim
CG3304	–	–	Damuda Group	Kamling	Sikkim
CG3305	–	–	Damuda Group	Reshi	Sikkim
CG3306	–	–	Damuda Group	Reshi	Sikkim

Notes: “–” means “Not reported”

CG3306 were collected near the Reshi Khola in the Reshi town (Ghosh et al. 2018a, 2020). These coals belong to the Damuda Group of the Gondwana Supergroup. CG3300, CG3301, and CG3302 samples outcropped on the foreland dipping Jorethang horse of the Rangit duplex in the south of the Rangit window, whereas CG3303 outcropped on the Namchi horse. CG3304, CG3305, and CG3306 samples were collected from the hinterland dipping horses of the Rangit duplex in the north of the Rangit window. As these areas are extremely close to international borders, detailed information of sample locations is kept confidential. All the coal samples were preserved within high-quality bags that protected the samples from contamination, additional moisture, and sample loss. At the laboratory, the samples were air-dried at 40 °C for 3 h following the standard guidelines mentioned in ISO 18283 (2006).

### 3.2 X-ray fluorescence (XRF)

The samples were ground and sieved to -212 micron size and were kept within open crucibles in a furnace at  $815 \pm 10$  °C temperature for 1 h to obtain the ash yield. The ash yield values in the analytical state were calculated following ASTM (2015) standard. After that, 5 mg of the ash samples were mixed thoroughly with a drop of paraffin for making a compact mixture. Then, that mixture was spread as a 3 mm thick layer over a very thin layer of boric acid ( $H_3BO_3$ ). After that, a pressing machine was employed to press the mixtures with 20 tons weight for 1 min. Mylar foils of 1micron thickness were used to cover the pellets, and then, the covered samples were placed inside the X-ray fluorescence (XRF) instrument.

The authors had carried out the X-ray fluorescence study of these ash samples at the R&D Centre for Iron and Steel (RDCIS), Ranchi, India, with the aid of a Rikako Koyama XRF instrument. The repeatability and reproducibility of the results were 0.040%, and 0.075%, respectively.

### 3.3 Fourier transform infrared (FTIR) spectroscopy

To carry out the FTIR spectroscopy, the coal samples were treated following the methodologies described by Painter et al. (1981). First, the coal samples were ground and processed through a sieve having aperture of 74 microns (200 mesh). Then, 1 mg of the powdered coal samples were dehydrated initially within a vacuum for several hours. After that, the dried coal samples were combined with 100 mg of potassium bromide (KBr). Then, the samples and Kbr were mixed by grinding for approx. 30 s and subsequently pressed to form 13 mm diameter pellets in an evacuated die under the pressure of 130 MPa (Solomon and Carangelo 1982). These pellets were desiccated within a vacuum oven for at least 48 h to alleviate the influence of moisture on the infrared spectra. Thereafter, the dried pellets were scanned using a Bruker 3000 Hyperion Microscope compounded with a Vertex 80 FTIR system at the Sophisticated Analytical Instrument Facility in Indian Institute of Technology, Bombay (IITB) in Mumbai, India. The spectra were recorded within  $4000\text{--}400\text{ cm}^{-1}$  wavenumber region in absorbance mode. Ten spectra from each pellet (or each sample) were acquired to minimize any bias or error in the absorbance intensities. To minimize uncertainties in the absorbance intensities, those spectra were compared.



However, negligible uncertainties and shifts ( $<0.05 \text{ cm}^{-1}$ ) in the absorbance intensities were observed. So, all the spectra exhibited almost similar absorbance characteristics for a particlaur sample. Then, a representative raw infrared spectrum for each sample was considered for the spectral deconvolution. Finally, the representative raw spectrum of each sample was curve-fitted using the Gaussian function in the FitYK 1.3.1 software.

## 4 Results

### 4.1 Major elemental oxide distributions in the ash yield of the studied coal samples

Table 5 represents the ranges of the concentrations of the major elemental oxides in the ash yield of the studied samples. In the ash yield, the silica ( $\text{SiO}_2$ ) content varies from 48.65 wt% to 65.09 wt% in bituminous coal samples, while it ranges from 35.92 wt% to 50.11 wt% in the anthracite samples. The ranges of the  $\text{Al}_2\text{O}_3$  exhibit a steady variation between 25.07 wt% and 29.84 wt% in bituminous coal samples and 23.97 wt% to 31.22 wt% in the anthracite samples. The CaO content is drastically low in the ash yield of the anthracite samples (0.06 wt% to 0.49 wt%) in comparison to the bituminous coal samples (0.68 wt% to 4.49 wt%) (Fig. 5a). The  $\text{K}_2\text{O}$  content, on the other hand, shows higher concentration anthracite samples (4.78 wt% to 7.41 wt%) compared to that in the ash yield of the bituminous coal samples (0.88 wt% to 2.54 wt%) (Fig. 5b). The  $\text{Na}_2\text{O}$  and  $\text{P}_2\text{O}_5$  contents vary from 0.09 wt% to 0.39 wt% and 0.08 wt% to 4.29 wt%, respectively, in the bituminous coal samples, while 0.08 wt% to 0.20 wt% and 0.05 wt% to 3.22 wt%, respectively, in the anthracite samples. Further, the FeO, MgO, and MnO concentrations in the ash yield range from 4.49 wt% to 6.45 wt%, 0.47 wt% to 2.04 wt% and 0.010 wt% to 0.063 wt%, respectively in the bituminous coal samples, whereas from 1.72 wt% to 12.43 wt%, 0.50 wt% to 2.79 wt% and 0.02 wt% to 0.12 wt%, respectively, in the anthracite samples. The  $\text{TiO}_2$  content ranges between in the anthracite 1.31 wt% and 2.32 wt% in the anthracite samples compared to that in the bituminous coal samples (1.54 wt% to 4.22 wt%). The  $\text{Al}_2\text{O}_3/\text{TiO}_2$  ratio varies from 6.97 to 17.02 in the bituminous coal samples, whereas 10.33 to 20.06 in the anthracite samples. Further,  $\text{K}_2\text{O}/\text{Al}_2\text{O}_3$  ratio ranges from 0.03 to 0.09 in the ash yield of the bituminous coal samples, whereas between 0.16 and 0.27 in the anthracite samples. The index of compositional variation (ICV) values exhibit variation from 7.00 to 15.14 in the ash yield of the bituminous coal samples, whereas from 5.91 to 10.57 in the ash yield of the anthracite samples. Moreover, the plagioclase index of alteration (PIA) and the chemical index of alteration (CIA) values vary from 76.94 to 98.91 and 73.73 to 95.66, respectively, in the bituminous coal samples, while from 93.20 to 98.29 and

75.79 to 81.52, respectively, in the anthracite samples. Finally, the palaeohumidity factor (PHF) varies from 0.56 to 1.75 in the bituminous coal samples, whereas between 0.25 and 1.50 in the anthracite samples.

### 4.2 Fourier transform infrared (FTIR) spectroscopy

The fitted Fourier transform infrared peaks are assigned following the works of Djomgoue and Njopwouo (2013), Saikia and Parthasarathi (2010), and Varma et al. (2018) and the representative fitted curves from the bituminous (CG 1674), and the anthracite samples (CG3303) are displayed in Fig. 6a–f. The fitted spectra in the bituminous coal samples exhibit the stretching frequencies of kaolinite at around 3620, 3651, 3671, and 3691  $\text{cm}^{-1}$  (Fig. 6a), where the first one is related to the inner —OH stretching vibrations of the kaolinite structure and the last three peaks correspond to the vibrations of the surface hydroxyls (Saikia and Parthasarathi 2010). Additionally, the peak near 3420  $\text{cm}^{-1}$  (Fig. 6a) may be attributed to the H—O—H stretching mode of water present within the montmorillonite clay (Djomgoue and Njopwouo 2013). Moreover, the peaks near 1008 and 1030  $\text{cm}^{-1}$  (Fig. 6b) may represent the presence of quartz and feldspar (Varma et al. 2018) in these samples. Besides, the —OH bending vibrations of the kaolinite (Fig. 6c) are found around 940  $\text{cm}^{-1}$  (surface —OH bending), 913  $\text{cm}^{-1}$  (inner surface —OH bending), and 754  $\text{cm}^{-1}$  (surface —OH bending) (following Saikia and Parthasarathi 2010). Further, the —OH bending vibration of montmorillonite is observed near 695  $\text{cm}^{-1}$ . The Si—O—Si inter-tetrahedral bridging bonds in  $\text{SiO}_2$  (Fig. 6c) are observed near 780 and 798  $\text{cm}^{-1}$  (Saikia and Parthasarathi 2010).

On the other hand, the hydroxyl stretching peaks of kaolinite exhibit irregular appearances in the anthracite samples except the inner hydroxyl stretching intensity around 3620  $\text{cm}^{-1}$  (Fig. 6d). The —OH stretching frequency of illite near to 3600  $\text{cm}^{-1}$  is observed in these samples (Fig. 5d) (Djomgoue and Njopwouo 2013). The peaks of quartz and feldspar (Fig. 6e) along with that of the Si—O—Si inter-tetrahedral bridging bonds of  $\text{SiO}_2$  are also observed in the anthracite samples (Fig. 6f). Apart from these peaks, the bending intensities of kaolinite are observed around 754  $\text{cm}^{-1}$  and 912  $\text{cm}^{-1}$ , corresponding to the surface hydroxyl and inner surface —OH bending vibrations (Fig. 6f).

## 5 Discussions

### 5.1 Major elemental oxides

#### 5.1.1 Inorganic parent rock composition

The  $\text{SiO}_2$  content in the ash yield of the studied samples may imply intermediate igneous source rocks with slight

**Table 5** Rank, disposition of major elemental oxides, their ratios as well as the indices computed from those disposition within the ash yield of the studied samples

Serial No.	Sample No.	$\bar{R}_t$ (%)	Rank	SiO <sub>2</sub>	Al <sub>2</sub> O <sub>3</sub>	Na <sub>2</sub> O	CaO	K <sub>2</sub> O	MgO	Fe <sub>2</sub> O <sub>3</sub>	MnO	TiO <sub>2</sub>	P <sub>2</sub> O <sub>5</sub>	K <sub>2</sub> O/Na <sub>2</sub> O	Al <sub>2</sub> O <sub>3</sub> /TiO <sub>2</sub>	K <sub>2</sub> O/Al <sub>2</sub> O <sub>3</sub>	ICV	PIA	CIA	PHF
1	CG1671	0.65	Bituminous C*	59.22	25.07	0.39	2.19	2.48	2.04	5.07	0.04	1.56	1.44	6.36	15.99	0.09	7.00	82.87	77.41	0.88
2	CG1672	0.58	Bituminous D*	60.71	26.19	0.18	0.68	2.06	1.57	6.45	0.03	1.53	0.08	11.44	17.03	0.078	6.43	97.58	90.25	1.66
3	CG1673	0.95	Bituminous C*	48.65	29.43	0.18	4.44	1.37	0.80	5.97	0.06	4.22	3.71	7.61	6.97	0.04	15.14	76.94	74.90	1.37
4	CG1674	1.09	Bituminous B*	64.09	28.07	0.09	0.80	1.05	0.49	1.49	0.01	3.03	0.10	11.67	9.24	0.03	11.20	98.91	95.14	1.59
5	CG1675	0.90	Bituminous C*	60.63	28.01	0.14	0.68	2.10	0.88	3.81	0.03	2.73	0.20	15.00	10.24	0.07	10.24	98.23	91.09	1.50
6	CG1676	0.76	Bituminous C*	57.50	26.02	0.21	2.54	2.01	1.73	5.71	0.04	1.94	1.60	9.57	13.41	0.07	8.18	97.16	90.06	1.11
7	CG1677	1.00	Bituminous B*	61.13	29.84	0.12	1.22	0.88	0.53	2.50	0.01	2.94	0.17	7.33	10.12	0.02	10.27	98.63	95.66	1.75
8	CG1679	1.00	Bituminous B*	55.60	27.86	0.19	3.87	2.54	0.46	2.36	0.01	2.14	4.29	13.37	13.02	0.09	8.27	77.76	73.73	0.56
9	CG3300	5.12	Anthracite A <sup>#</sup>	47.73	25.07	0.12	0.06	6.39	1.51	12.42	0.09	1.30	0.05	53.25	19.18	0.25	6.07	98.29	77.61	0.25
10	CG3301	4.94	Anthracite A <sup>#</sup>	48.95	29.11	0.16	0.08	4.78	1.41	7.70	0.10	1.45	0.19	29.88	20.07	0.16	5.61	93.20	80.81	1.50
11	CG3302	5.15	Anthracite A <sup>#</sup>	46.99	26.78	0.14	0.35	4.88	2.79	10.16	0.09	1.35	0.17	34.86	19.78	0.18	5.91	94.00	80.10	1.13
12	CG3303	5.36	Anthracite A <sup>#</sup>	47.14	28.44	0.20	0.48	6.59	2.12	7.20	0.11	1.76	0.20	32.95	16.15	0.23	6.95	96.95	78.49	1.26
13	CG3304	4.11	Anthracite A <sup>#</sup>	50.11	31.21	0.15	0.36	5.70	0.76	2.94	0.02	1.84	0.29	38.00	16.89	0.18	6.38	96.48	81.52	0.85
14	CG3305	4.15	Anthracite A <sup>#</sup>	35.92	23.97	0.08	0.32	6.41	1.48	9.25	0.02	2.31	3.22	80.13	10.34	0.26	10.57	95.90	75.79	0.57
15	CG3306	4.73	Anthracite A <sup>#</sup>	44.13	28.02	0.17	0.16	7.41	0.50	1.72	0.03	1.96	0.06	43.59	14.28	0.26	7.52	97.19	76.54	1.21

Notes:  $\bar{R}_t$  (%) refers to Mean random vitrinite reflectance; ICV refers to Index of compositional variation; PIA refers to Plagioclase index of alterations; CIA refers to Chemical index of alterations; PHF refers to Palaeohumidity factor; \* means Mentioned in Anwita et al. (2020) and Ghosh et al. (2020), # means Mentioned in Anwita et al. (2020), Ghosh et al. (2018a, 2020); all major oxide concentrations are mentioned in wt%, unless indicated.

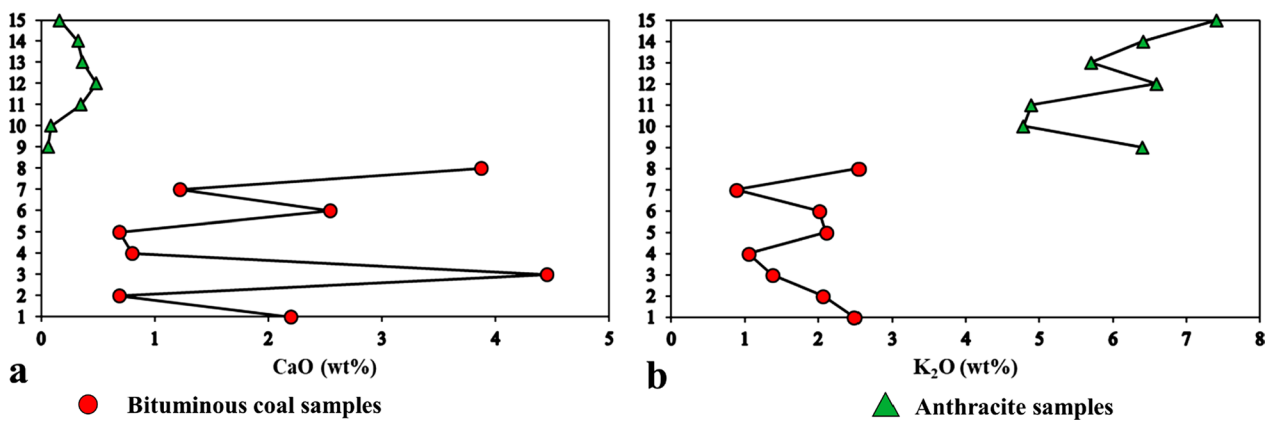


**Fig. 5** Low CaO content **a** and high K<sub>2</sub>O content in the anthracite samples **b**. *Notes:* The Y-axis in both of the plots represents the serial number of the samples mentioned in Table 5. 1—CG1671, 2—CG1672, 3—CG1673, 4—CG1674, 5—CG1675, 6—CG1676, 7—CG1677, 8—CG1679, 9—CG3300, 10—CG3301, 11—

CG3302, 12—CG3303, 13—CG3304, 14—CG3305, 15—CG3306. The repeatability and reproducibility of the all the oxide data were approx. 0.04%, and approx. 0.075%, respectively, with negligible error in data treatment

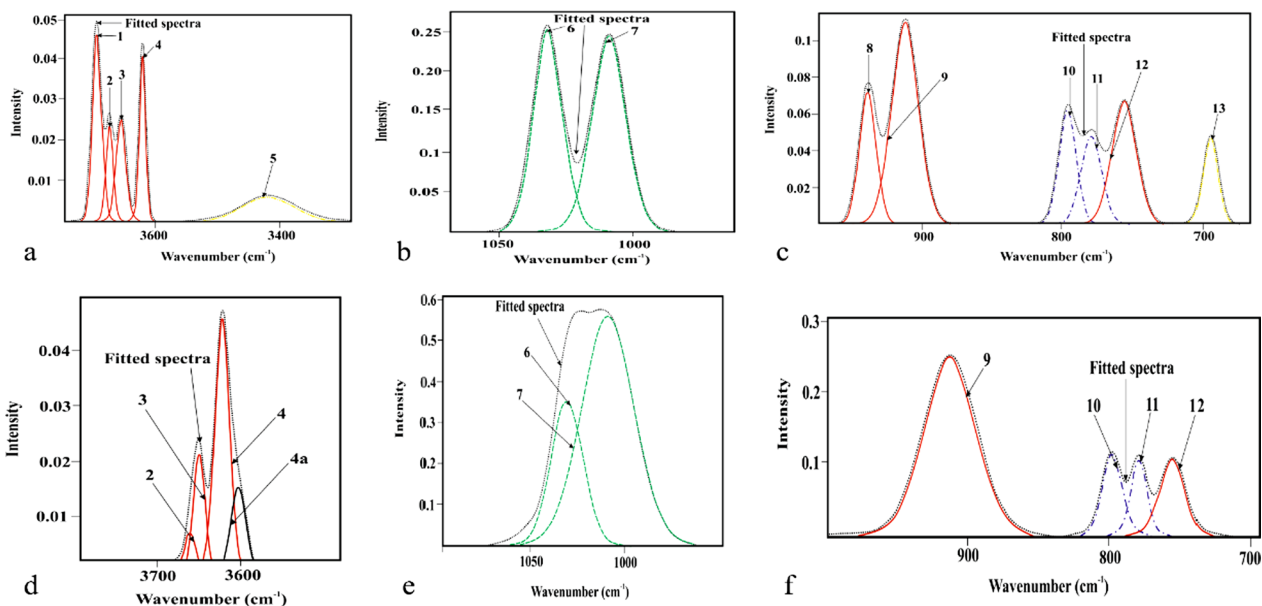


**Fig. 6** **a** OH stretching vibrations of kaolinite and montmorillonite, **b** Vibrational frequencies of quartz and feldspar, **c** OH bending vibrations of kaolinite and montmorillonite as well as Si–O–Si inter-tetrahedral bridging bonds of SiO<sub>2</sub> in CG1674 (representative sample of the bituminous coal sample set), **d** OH stretching vibrations of kaolinite and illite, **e** Vibrational frequencies of quartz and feldspar, **f** OH bending vibrations of kaolinite as well as Si–O–Si inter-tetrahedral bridging bonds of SiO<sub>2</sub> in CG3303 (representative sample of the anthracite sample set). *Notes:* 1: Surface —OH stretching vibration of kaolinite, 2: Surface —OH stretching vibration of kaolinite, 3: Sur-

face —OH stretching vibration of kaolinite, 4: Inner surface —OH stretching vibration of kaolinite, 5: H–O–H stretching vibrations of water within montmorillonite, 6: Quartz, 7: Quartz, and feldspar, 8: Surface —OH bending vibration of kaolinite, 9: Inner surface —OH bending vibration of kaolinite, 10: Si–O–Si inter-tetrahedral bridging bonds of SiO<sub>2</sub>, 11: Si–O–Si inter-tetrahedral bridging bonds of SiO<sub>2</sub>, 12: Surface —OH bending vibration of kaolinite, 13: —OH bending vibration of montmorillonite. Peaks are assigned following the works of Djomgoue and Njopwouo (2013), Saikia and Parthasarathi (2010) and Varma et al. (2018)

inputs from the mafic and felsic ends as well. However, the variation in silica concentrations in the two sample sets may be due to the disparities in its origin from the source minerals (quartz, feldspars, and clays). The sum of MgO and Fe<sub>2</sub>O<sub>3</sub> contents vary from 1.99 wt% to 8.02 wt% in the ash

yield of the bituminous coal samples, while in the ash yield of the anthracite samples, the range is between 2.23 wt% and 13.95 wt%. The range of the sum of these two major elemental oxides may, further, imply the input from igneous rocks of intermediate composition. Additionally, the ratio of

$\text{Al}_2\text{O}_3$  to the  $\text{TiO}_2$  ( $\text{Al}_2\text{O}_3/\text{TiO}_2$ ) can discriminate the source rock characteristics of the clastic sediments. The range of this ratio from 3 to 8 implies the mafic igneous rocks; 8 to 21 indicates intermediate igneous rocks, and 21 to 70 for felsic rocks (Hayashi et al. 1997). The range of this ratio (Table 5) in the bituminous coal samples may indicate the dominant input from intermediate igneous rocks with a little influence from the mafic igneous rocks (Fig. 7a). This ratio may additionally suggest that the minerals in the anthracite samples would have also derived from the igneous rocks of intermediate composition with a little influence from felsic sources (Fig. 7a).

The  $\text{P}_2\text{O}_5$  and the CaO are strongly correlated ( $R=0.97$ ) in the bituminous coal samples (Fig. 7b), which may indicate the formation of apatite. In the anthracite samples, these two parameters show a moderate correlation ( $R=0.65$ ) (Fig. 7b). CG3305 contains a large amount of  $\text{P}_2\text{O}_5$ , which leads to the exclusion of this particular sample from the bivariate plot of the  $\text{P}_2\text{O}_5$  and CaO for the anthracite samples.

### 5.1.2 Palaeohumidity

The distribution and abundance of some chemical elements may provide imperative clues regarding the palaeoenvironmental conditions that prevailed during the sediment deposition (Moradi et al. 2016; Worash 2002) in the peatland. The humid climatic condition enriches Fe, Mn, Cr, V, Ni, and Co (Cao et al. 2012). On the other hand, under arid condition, the rate of evaporation overcomes the rate of precipitation, enhancing the alkalinity of water, which in turn, leads to the enrichment of Mg, Ca, Na, K, Ba and Sr. Cao et al. (2012), Moradi et al. (2016) and Zhao et al. (2007) among others

had applied the C-value (Eq. (1)) as a proxy to document the transformations in palaeoclimate:

$$C = (\text{Fe} + \text{Mn} + \text{Cr} + \text{Ni} + \text{V} + \text{Co}) / (\text{Ca} + \text{Mg} + \text{Sr} + \text{Ba} + \text{K} + \text{Na}) \quad (1)$$

However, the trace elements are not detected in this study. Therefore, a new index, termed as palaeohumidity factor (PHF), is proposed in this study, which considers only the Fe, Mn, and Ti in the numerator, while Ca, Mg, Na, and K in the denominator. All the concentrations are considered as elemental weight percentages. The PHF is calculated (Eq. (2)) as follows:

$$\text{PHF} = (\text{Fe} + \text{Mn} + \text{Ti}) / (\text{Ca} + \text{Mg} + \text{K} + \text{Na}) \quad (2)$$

The range of the PHF in the bituminous coal samples lies between 0.56 and 1.75, whereas in the anthracite A samples, this parameter ranges from 0.25 to 1.50 (Table 5). Most of the samples may indicate the sub-humid to humid climatic conditions (Fig. 8).

### 5.1.3 Clay mineral composition

**5.1.3.1  $\text{K}_2\text{O}/\text{Al}_2\text{O}_3$  ratio** Cox et al. (1995) had observed the ratio of  $\text{K}_2\text{O}$  to  $\text{Al}_2\text{O}_3$  ( $\text{K}_2\text{O}/\text{Al}_2\text{O}_3$ ) lies between 0 and 0.3 in clay minerals, while between 0.3 and 0.9 in feldspars and close to zero in the sediments comprising a large amount of kaolinite, montmorillonite, saponite, and halloysite, etc. In illite-rich sediments, this ratio varies from 0.2 to 0.3 (Cox et al. 1995). The range of this ratio (Table 5) in the bituminous coal samples may imply the presence of an abundant amount of kaolinite (most dominant), vermiculite, montmorillonite clays (Fig. 9a). In the anthracite samples, this ratio

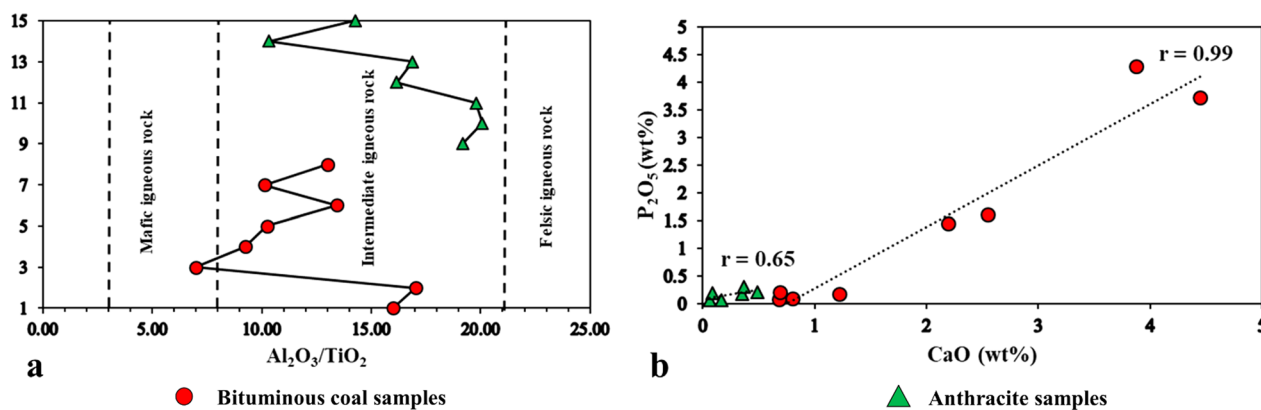


**Fig. 7** **a**  $\text{Al}_2\text{O}_3/\text{TiO}_2$  ratio of the studied samples showing the source rock composition; **b** CaO versus  $\text{P}_2\text{O}_5$  plot showing formation of apatite in the samples. CG3305 is excluded from (b) due to the high  $\text{P}_2\text{O}_5$  content, which was influencing the correlation. The Y-axis in (a) represents the serial number of the samples mentioned in Table 5. 1—CG1671, 2—CG1672, 3—CG1673, 4—CG1674, 5—CG1675, 6—CG1676, 7—CG1677, 8—CG1679, 9—CG3300, 10—CG3301, 11—CG3302, 12—CG3303, 13—CG3304, 14—CG3305, 15—

CG3306. The repeatability and reproducibility of the all the oxide data were approx. 0.04%, and approx. 0.075%, respectively, with negligible error in data treatment. The coefficient of regression ( $R^2$ ) values of the correlation between the CaO and  $\text{P}_2\text{O}_5$  (Fig. 7b) for the bituminous and anthracite samples are 0.94, and 0.42, respectively. The standard error values of the correlation between the CaO and  $\text{P}_2\text{O}_5$  (Fig. 7b) for the bituminous and anthracite samples are 0.45, and 0.07, respectively.



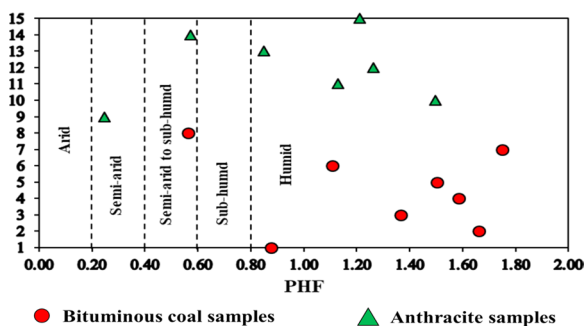


**Fig. 8** Palaeohumidity factor (PHF) showing sub-humid to humid climatic conditions. *Notes:* The Y-axis in this plot represents the serial number of the samples mentioned in Table 5. 1—CG1671, 2—CG1672, 3—CG1673, 4—CG1674, 5—CG1675, 6—CG1676, 7—CG1677, 8—CG1679, 9—CG3300, 10—CG3301, 11—CG3302, 12—CG3303, 13—CG3304, 14—CG3305, 15—CG3306

(Table 5) may indicate the presence of kaolinite, montmorillonite, and illite (Fig. 9a).

**5.1.3.2 Index of compositional variation (ICV)** In complementary, the index of compositional variation (ICV; Eq. (3)) proposed by Cox et al. (1995) can differentiate the characters of the source rocks based on the concentration of the major elemental oxides:

$$ICV = (Fe_2O_3 + K_2O + CaO + Na_2O + MgO + MnO + TiO_2) / Al_2O_3 \tag{3}$$

This index measures the concentration of alumina with respect to the other major elemental oxides, and it excludes SiO<sub>2</sub> to avoid the problems of quartz dilution (Cox et al. 1995). The non-clay silicates comprise comparatively

smaller amounts of alumina than the clay minerals and hence, show larger ICV values than the clays. Additionally, the amphiboles and the pyroxenes exhibit larger ICV values as they are more prone to chemical weathering on the earth's crust, while relatively stable mineral-like alkali feldspar shows lower ICV. This index further lowers in montmorillonite and illite and becomes the lowest in the kaolinite minerals (Cox et al. 1995). In the present study, the ICV values in the bituminous and the anthracite samples range from 0.25 to 0.58 and 0.38 to 0.87, respectively (Table 5). The range of the ICV in the bituminous coal samples may imply the mixed abundance of kaolinite and montmorillonite clays (Fig. 9b), whereas, in the anthracite samples, this index may suggest mainly the presence of illite (Fig. 9b) mixed with kaolinite.

**5.1.4 Weathering extent of the inorganic parent rocks**

The Plagioclase index of alteration (PIA) was calculated (Eq. (4)) following Fedo et al. (1995) to document the degree of chemical weathering of the plagioclase feldspar.

$$PIA = 100 \times (Al_2O_3 - K_2O) / [(Al_2O_3 - K_2O) + CaO^* + Na_2O] \tag{4}$$

Here, the major element concentrations are consid-

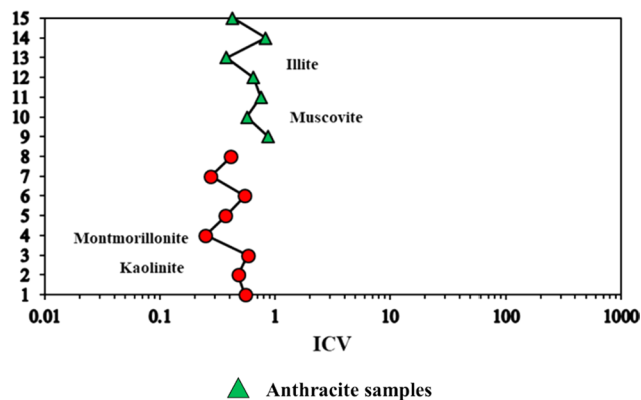
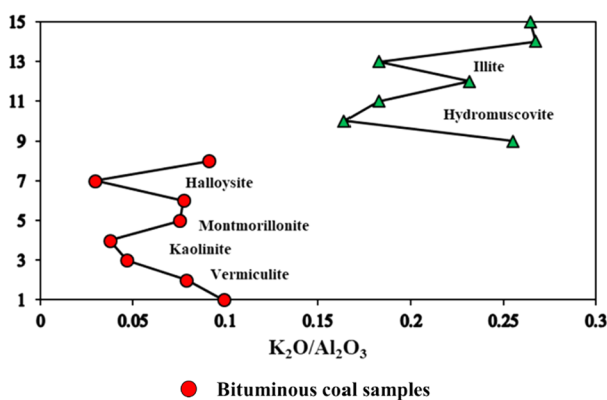


**Fig. 9 a** Relation between the K<sub>2</sub>O and Al<sub>2</sub>O<sub>3</sub> contents, **b** Index of compositional variation (ICV) discriminating the type of clay mineral present in the samples. The ranges of the K<sub>2</sub>O/Al<sub>2</sub>O<sub>3</sub> and the ICV values have been mentioned following Cox et al. (1995). The Y-axis in both of the plots represents the serial number of the samples mentioned in Table 5. 1—CG1671, 2—CG1672, 3—CG1673, 4—

CG1674, 5—CG1675, 6—CG1676, 7—CG1677, 8—CG1679, 9—CG3300, 10—CG3301, 11—CG3302, 12—CG3303, 13—CG3304, 14—CG3305, 15—CG3306. The repeatability and reproducibility of the all the oxide data were approx. 0.04%, and approx. 0.075%, respectively, with negligible error in data treatment

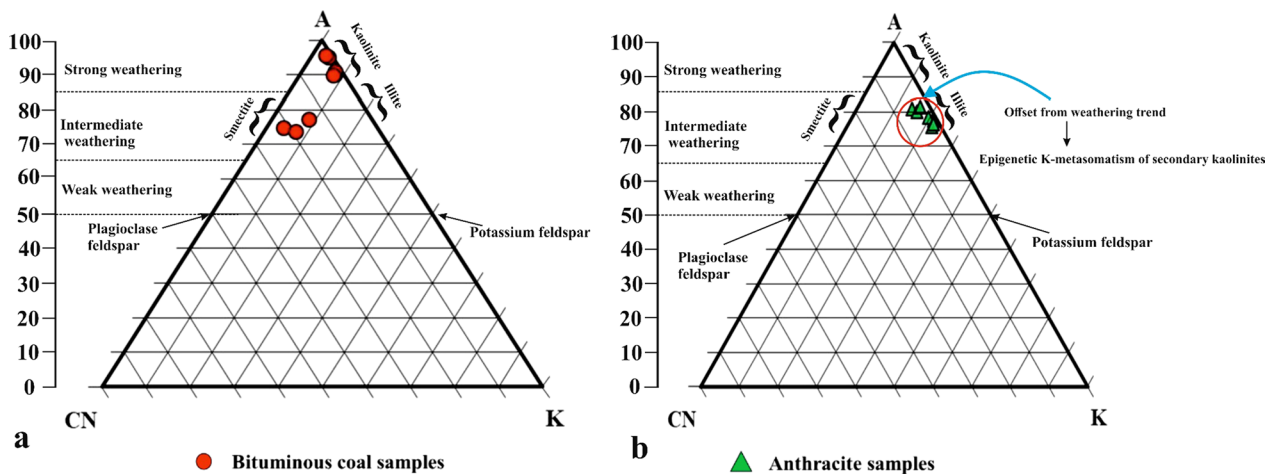


**Fig. 10** **a** Bituminous coal samples are plotted in the A–CN–K ( $\text{Al}_2\text{O}_3\text{--CaO}^* + \text{Na}_2\text{O--K}_2\text{O}$ ) diagram with three samples (CG1671, CG1673, and CG1679) lying near smectite (montmorillonite) field, **b** Anthracite samples are plotted in the A–CN–K

( $\text{Al}_2\text{O}_3\text{--CaO}^* + \text{Na}_2\text{O--K}_2\text{O}$ ) diagram near the field of illite showing offset from the common weathering trend and the plausible influence of potassium-metasomatism (K-metasomatism) (adapted from Bai et al. 2015)

( $\text{CaO}_{\text{corrected}} = \{\text{CaO} - (3.33 \times \text{P}_2\text{O}_5)\}$ ) remains  $> \text{Na}_2\text{O}$ , then the  $\text{CaO}^*$  equals the value of the  $\text{Na}_2\text{O}$ . But the  $\text{CaO}^*$  equals the concentration of the  $\text{CaO}$  if the  $\text{CaO}_{\text{corrected}}$  is less than the concentration of the  $\text{Na}_2\text{O}$ . This index shows the variation from 76.94 to 98.91 and from 93.19 to 98.29 (Table 5) in the bituminous and the anthracite samples, respectively. Therefore, these values may imply the moderate to intense chemical weathering of plagioclase feldspar in both sample sets. The smaller values of this ratio in CG1671, CG1673, and CG1679 would have resulted possibly due to the presence of reasonable amounts of smectite class of clay, which includes, especially, the montmorillonite.

The chemical index of alteration (CIA) proposed by McLennan et al. (1993) may potentially indicate the degree of chemical weathering on the earth's crust that the parent rocks had experienced, which may, in turn, point towards the palaeohumidity conditions. The high CIA values may indicate strong chemical weathering triggered by warm and moist climate, while the low CIA values may imply weak chemical weathering under cold and arid conditions. The CIA is calculated (Eq. (5)) as below:

$$\text{CIA} = \left[ \frac{\text{Al}_2\text{O}_3}{\text{Al}_2\text{O}_3 + \text{CaO}^* + \text{Na}_2\text{O} + \text{K}_2\text{O}} \right] \times 100 \quad (5)$$

Here,  $\text{CaO}^*$  is obtained from the method described by McLennan et al. (1993) and in the same method mentioned for the calculation of PIA. The CIA values for the bituminous coal samples vary from 73.73 to 95.66 (Table 5). CG1671, CG1673, and CG1679 samples have comparatively lower CIA values and plot near the smectite field of the A–CN–K diagram (Fig. 10a). This may suggest the presence of considerable amounts of montmorillonite (a subclass of smectite) that would have led to plot these three samples

along the A–CN axis. The rest of the bituminous coal samples show larger CIA values indicating strong chemical weathering under hot and humid climatic conditions and consequently a large amount of kaolinite that might have caused the samples to lie at the  $\text{Al}_2\text{O}_3$  apex (Fig. 10a).

### 5.1.5 Epigenetic potassium metasomatism

The chemical index of alteration (CIA) parameter ranges between 75.79 and 81.52 in the anthracite samples (Table 5), which may apparently imply moderate chemical weathering under warm and moist conditions. Interestingly, these samples cluster along the A–K axis near the illite field within the A–CN–K diagram and plot a bit offset from the traditional weathering trend (Fig. 10b), which may indicate the plausible influence of potassium metasomatism (K-metasomatism) in these anthracite samples. Ghosh et al. (2018a) related the metamorphic degree of these anthracite samples to the onset of the greenschist facies metamorphism as indicated by the peak paleotemperature (334.94–369.01 °C) calculated from the mean random vitrinite reflectance, and the peak metamorphic temperature (325.12–387.89 °C) estimated from the Raman spectroscopy. The greenschist facies metamorphism takes place at temperature of approx. 300–500 °C and pressure of approx. 3–20 kbar (Arndt 2011). So, although the extent of tectonic pressure was not estimated, the temperature ranges of the anthracite samples almost match with that of the greenschist facies.

Now, during metamorphism, the breakdown of the volatile-bearing minerals originates the metamorphic fluids, which may play important roles in bringing metasomatic changes. The migration of metamorphic fluid requires interconnected porosity and permeability, which may be

primary (intrinsic) or secondary (tectonism and deformation-induced). In general, the metamorphic rocks comprise low interconnected porosity and permeability (Ague 2003; Etheridge et al. 1984; Manning and Ingebritsen 1999; Oliver 1996) and thus, any tectonic deformation may enhance the fluid intrusions in the metamorphic rocks through developing weak planes (Putnis and Austrheim 2010; Yardley et al. 2000). Therefore, structurally weak planes, like the shear zones, fault planes, and fold axes developed during the tectonism and consequent deformation (Abart et al. 2002; Gupta and Bickle 2004; McCaig et al. 1995; Pitcairn et al. 2010; Selverstone et al. 1992; Skelton et al. 1995) offer the plausible routes for the movement of metamorphic fluids.

The Himalayan deformation episodes would have also introduced secondary fractures, joints, pores, etc. in these anthracite coals, which possibly played crucial roles in bringing metasomatic alterations in these samples. Besides, during the transitions in pressure and temperature in metamorphic course, metamorphic fluids may experience complex changes in chemical compositions. Interactions with the host rocks may also alter the chemical properties of these fluids. Such metamorphic fluid of a complex origin and with large potassium content would have penetrated through the secondary weak planes (fractures, joints and pores, etc.) in the studied anthracite samples and induced the epigenetic potassium metasomatic transformations. Additionally, according to GSI (2012), the Gondwana sequence in the Damuda Formation was intersected by the ultrapotassic lamprophyre sill. So, it may also be possible that hydrothermal fluid with large  $K_2O$  concentration originated from this lamprophyre sill would have migrated through the secondary weak planes of the anthracite coals and brought about the potassium (K) metasomatism.

Fedo et al. (1995) had reported the effects of K-metasomatism of sandstone. The K-metasomatism either may transform the aluminous clay minerals like kaolinites to illites or convert the plagioclase feldspar to K-feldspar. These two processes have different effects on the CIA values. The first pathway results in low CIA than the pre-metasomatized rocks, while the second route leads to unaltered CIA values. Although, both of these pathways enrich the potassium concentration in the metasomatized rocks (Fedo et al. 1995). In this investigation, the ICV values and the  $K_2O/Al_2O_3$  ratio of the anthracite samples reveal the abundance of illite mixed with kaolinite and montmorillonite; instead of showing the presence of the K-feldspar (Fig. 9a, b). Therefore, the epigenetic K-metasomatism is assumed here to take place through converting the kaolinites into illites. Further, along with the large  $K_2O$  content, high  $K_2O/Na_2O$  ratio may also signify the metasomatic effects (Brooks 1986). The  $K_2O/Na_2O$  ratio in the anthracite samples is high to very high (29.88–80.13) compared to that of the bituminous coal samples (6.36–15.00; Table 5), which may additionally suggest

the influence of K-metasomatism on the mineralogical compositions of the anthracite samples. Therefore, the K-metasomatism induced by metamorphic/hydrothermal fluid of high potassium content migrating through secondary weak planes would have acted as an epigenetic phenomenon to alter the clay mineralogical characteristics of these anthracite samples. However, all the kaolinites did not convert to illite as the flow of the metamorphic/hydrothermal fluid was possibly restricted by low interlayer spacing, as well as hydrophobicity developed by the aromatic stacking and polycondensation at the anthracite rank.

In this study, the CIA has been plotted against the PIA to observe whether these two proxies can jointly determine the degree of chemical weathering of the source rocks. These two parameters, in the bituminous coal samples, are highly correlated ( $R=0.98$ ) (Fig. 11), which may imply that these two weathering indices are in good agreement in revealing the intensity of chemical weathering of the parent inorganic rocks. Interestingly, in the anthracite samples, these two proxies show inverse correlation ( $R=-0.52$ ) (Fig. 11), suggesting the plausible influences of the epigenetic mineralogical alterations on these weathering indices. Although the PIA values reveal the strong chemical weathering of the plagioclase feldspar, the epigenetic K-metasomatism may offset these samples from the common weathering trend as reflected from the A–CN–K diagram and the CIA values, and that's why the CIA inversely correlates with the PIA. Therefore, the above discussion may suggest that the K-metasomatism would have altered substantial amounts of kaolinite to illite in the anthracite samples, which is in good agreement with the  $K_2O/Al_2O_3$  ratio and the ICV values.

#### 5.1.6 Estimation of quartz and kaolinite in the samples

The high-temperature chemical transformations of minerals like silicate, carbonate, sulfide, sulfate, oxides, etc., produce the ash in the coal. X-ray fluorescence spectroscopy of high-temperature ash (HTA) obtained from the bulk coal samples

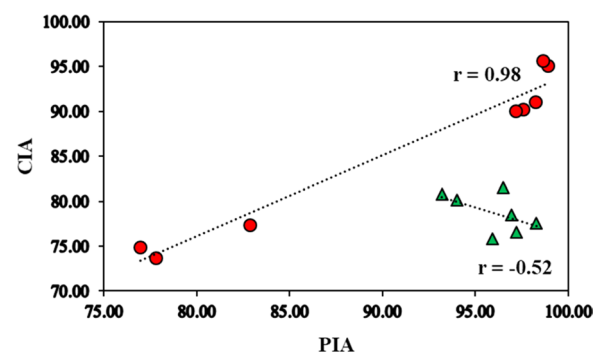


Fig. 11 Relation between the chemical index of alteration (CIA) and the plagioclase index of alteration (PIA) of the studied samples

can be used to calculate the quartz content in bituminous and anthracite samples based on the observations that quartz remains unaltered during ashing at high degree, unlike many minerals that undergo crystallographic or chemical alterations (Bandopadhyay 2010). The oxides like silica ( $\text{SiO}_2$ ) and alumina ( $\text{Al}_2\text{O}_3$ ) found in the X-Ray fluorescence spectroscopy of high-temperature coal-ash can be employed to estimate the quartz content in the bulk coal. The quartz content in high temperature-ash yield of coal samples can be calculated from the  $\text{SiO}_2$  and  $\text{Al}_2\text{O}_3$  contents from an empirical formula proposed by Raask (1985) and later modified by Bandopadhyay (2010) for Indian coals (Eq. (6)):

$$(\text{SiO}_2)_Q = (\text{SiO}_2)_t - 1.3 \times (\text{Al}_2\text{O}_3) \quad (6)$$

where  $(\text{SiO}_2)_Q$  is the percentage of silica in ash-yield,  $(\text{SiO}_2)_t$  is the percentage of total silica obtained in XRF analysis and  $\text{Al}_2\text{O}_3$  represents the weight-percentage of alumina derived from XRF analysis of the coal samples. Further, following the work of (Bandopadhyay 2010), the quartz content in bulk coal was computed from Eq. (7):

$$Q_C = 0.01 \times A^a \times (\text{SiO}_2)_Q \quad (7)$$

where,  $Q_C$  refers to quartz content in bulk coal sample;  $A^a$  refers to ash yield of coal in analytical state and  $(\text{SiO}_2)_Q$  refers to the percentage of silica in ash-yield.

Kaolinite content in the coal ash can also be determined from  $\text{SiO}_2$ ,  $\text{Al}_2\text{O}_3$ ,  $\text{K}_2\text{O}$ , potassium aluminosilicates, and quartz content following Raask's method (Raask 1985):

The potassium aluminosilicate ( $\text{K}_{\text{Al-Si}}$ ) present within the coal mineral matter can be calculated from the following Eq. (8):

$$\text{K}_{\text{Al-Si}} = \text{K}_2\text{O}/0.11 = 9.1 \times \text{K}_2\text{O} \quad (8)$$

Then, the kaolinite content in the ash yield ( $\text{Kaol}_{\text{ash}}$ ) can be determined by (Eq. (9)):

$$\text{Kaol}_{\text{ash}} = \left[ (\text{SiO}_2 + \text{Al}_2\text{O}_3 + \text{K}_2\text{O}) - \left\{ (\text{SiO}_2)_Q + \text{K}_{\text{Al-Si}} \right\} \right] \quad (9)$$

After that, the kaolinite in bulk coal sample ( $\text{Kaol}_C$ ) can be estimated as (Eq. (10)):

$$\text{Kaol}_C = 0.01 \times A^a \times \text{Kaol}_{\text{ash}} \quad (10)$$

The quartz content in bituminous coal samples varies from 1.45 wt% to 7.88 wt%, while in the anthracite samples, it ranges between 2.39 wt% and 7.65 wt% (Table 6). On the other hand, the kaolinite content in the bituminous coal samples is placed between 5.47 wt% and 15.99 wt%, whereas in the anthracite samples, the kaolinite content exhibits variation from 1.61 wt% to 13.45 wt% (Table 6). Moreover, the kaolinite to quartz ratio ( $\text{Kaol}_C/Q_C$ ) in the bulk bituminous

coal samples varies from 1.41 to 5.44, while in the anthracite samples, this ratio ranges from 0.39 to 2.69 (Table 6).

The variation in the quartz content in both sample sets may imply the variable input concentrations of quartz from the source igneous source rocks as the metamorphic influences on quartz concentration are negligible. Extremely low quartz content in CG1673 and CG 3305 may be associated with very poor derivation of quartz from the parent rocks or derivation from the silica-deficient parent rocks. The  $\text{Kaol}_C/Q_C$  ratio in CG1673 is overestimated due to this low quartz content. The ratio, in the rest of the bituminous coal samples, exhibits almost a stable variation and shows the values  $> 1$ , which may imply the dominance of kaolinite over quartz content in the bulk coal (Fig. 12). However, in the case of anthracite samples, this ratio shows unstable variation, possibly due to molecular breakdown of kaolinite structure at high temperature (325.02 to 387.89 °C; Ghosh et al. 2018a) as well as epigenetic transformations of kaolinite to illite by plausible epigenetic K-metasomatism. Surprisingly, in CG3300, CG3305, and CG3306, the kaolinite/quartz ratio declines to less than 1, which may correspond to the lowering of the kaolinite content through epigenetic alterations compared to the stable quartz grains (Fig. 12).

## 5.2 Spectral evidence of potassium metasomatism

The presence of four hydroxyl ( $-\text{OH}$ ) stretching peaks of kaolinite in the bituminous coal samples (Fig. 5a) may suggest the preservation of molecular ordering of the kaolinite structure, which in turn may low metamorphic temperature and relatively unaltered mineralogical framework in these samples. Moreover, the presence of the  $-\text{OH}$  stretching vibrations of montmorillonite in the bituminous coal samples may support the discussions based on the  $\text{K}_2\text{O}/\text{Al}_2\text{O}_3$  ratio and the ICV values regarding the clay composition. Also, this substantiates the presence of the sericite class of clay present in these samples observed from the A-CN-K diagram (Fig. 10a).

The inconsistencies of the hydroxyl stretching peaks in the anthracite samples may be the consequences of the dehydroxylation and removal of  $\text{OH}^-$  ions from the kaolinite structure (Ghosh et al. 2020). The high thermal maturity ( $\bar{R}_r$  of 4.11%–5.36%) of the anthracite samples would have resulted in the molecular disordering of the kaolinite structure and led to the dehydroxylation process. Meanwhile, the consistent appearance of the inner hydroxyl stretching frequency may correspond to relatively strong hydrogen bond energy compared to the surface hydroxyls (Ghosh et al. 2020). Additionally, the irregular appearances of the kaolinite stretching peaks may also provide a clue to the K-metasomatism of kaolinites to illites, apart from the dehydroxylation. The appearance of the hydroxyl stretching frequency of illite in these samples (Fig. 6d) may strengthen



**Table 6** Ash yield (in the analytical state), amounts of quartz and kaolinite in ash yield and bulk coal samples along with amounts of potassium aluminosilicates present in the mineral matter of the studied samples and ratio of total kaolinite to quartz contents in the bulk coal samples

Sample No.	Ash yield <sup>a</sup>	(SiO <sub>2</sub> ) <sub>Q</sub>	Q <sub>C</sub>	K <sub>Al-Si</sub>	Kaol <sub>ash</sub>	Kaol <sub>C</sub>	Kaol <sub>C</sub> /Q <sub>C</sub>
CG1671	14.57	26.63	3.88	22.63	37.53	5.47	1.41
CG1672	18.00	26.66	4.80	18.82	43.50	7.83	1.63
CG1673	13.97	10.39	1.45	12.52	56.56	7.90	5.44
CG1674	28.54	27.60	7.88	9.58	56.05	16.00	2.03
CG1675	29.77	24.22	7.21	19.17	47.37	14.10	1.96
CG1676	21.00	23.67	4.97	18.32	43.56	9.15	1.84
CG1677	15.96	22.34	3.57	8.04	61.49	9.82	2.75
CG1679	27.40	19.38	5.31	23.13	43.50	11.92	2.24
CG3300	50.54	15.14	7.65	58.24	5.83	2.95	0.39
CG3301	47.62	11.10	5.29	43.50	28.24	13.45	2.54
CG3302	51.88	12.17	6.32	44.48	22.01	11.42	1.81
CG3303	50.97	10.16	5.18	59.98	12.04	6.14	1.18
CG3304	50.27	9.53	4.79	51.89	25.62	12.88	2.69
CG3305	50.26	4.76	2.39	58.33	3.21	1.61	0.67
CG3306	49.02	7.70	3.78	67.44	4.43	2.17	0.58

Notes: Ash yield<sup>a</sup> refers to ash yield in analytical state, (SiO<sub>2</sub>)<sub>Q</sub> refers to percentage of silica in ash-yield, (SiO<sub>2</sub>)<sub>t</sub> refers to percentage of total silica obtained in XRF analysis, Q<sub>C</sub> refers to quartz content in bulk coal sample, K<sub>Al-Si</sub> refers to potassium aluminosilicate (K<sub>Al-Si</sub>) present within the coal mineral matter, Kaol<sub>ash</sub> refers to kaolinite content in the ash yield, Kaol<sub>C</sub> refers to kaolinite in bulk coal sample, Kaol<sub>C</sub>/Q<sub>C</sub> refers to ratio of total kaolinite to quartz contents in the bulk coal samples

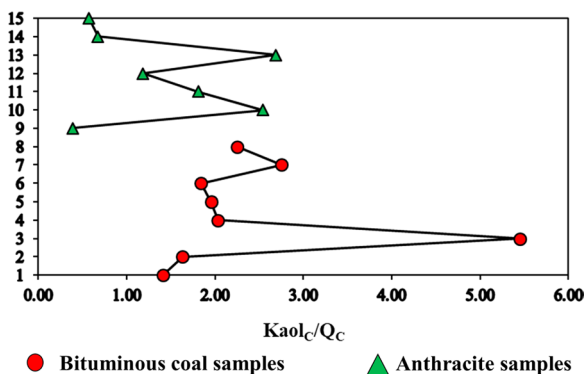


**Fig. 12** Ratio of total kaolinite to quartz contents within the bulk coal samples. The Y-axis in this plot represents the serial number of the samples mentioned in Table 5. 1—CG1671, 2—CG1672, 3—CG1673, 4—CG1674, 5—CG1675, 6—CG1676, 7—CG1677, 8—CG1679, 9—CG3300, 10—CG3301, 11—CG3302, 12—CG3303, 13—CG3304, 14—CG3305, 15—CG3306

this clue of the epigenetic K-metasomatism in the anthracite samples influencing the kaolinite molecular structure. This observation is, hence, in good agreement with the interpretations of the A–CN–K diagram (Fig. 10b). The absence of the two peaks of surface –OH bending of kaolinite (Fig. 6f) may be in good agreement with the thermal decomposition and K-metasomatism of kaolinites. The hydroxyl bending vibration of montmorillonite has not been observed in these samples.

From the deconvoluted FTIR spectra, the total hydroxyl stretching and bending intensities of the kaolinite and the

intensities of quartz and feldspar are calculated (Table 7). The total kaolinite intensity (TI<sub>K</sub>) is always less than the intensity of the quartz and feldspar (TI<sub>Q-F</sub>). Further, the ratio of these total intensities (TI<sub>K</sub>/TI<sub>Q-F</sub>) in the anthracite samples is found to decline from the bituminous coal samples (Fig. 13a), which may support the thermal decomposition and the K-metasomatism of the kaolinites to illites. For additional confirmation, this ratio has been correlated with the R<sub>r</sub> values, and it is observed that this ratio forms clusters within the reflectance range of the two sample sets (Fig. 13b) and varies non-linearly with the thermal maturity. This non-linear correlation of these two variables may suggest that the thermal maturity solely did not affect this ratio; instead, it was also influenced by epigenetic K-metasomatism to a significant extent.

### 6 Conclusions

- (1) The inorganic geochemical findings from the ash yield of the studied bituminous and anthracite samples have provided insights into the clay mineralogical framework and its alteration at the anthracite rank.
- (2) The clay mineralogical framework of the bituminous coal samples comprises kaolinite mixed with montmorillonite, and reveals moderate to strong weathering of the parent rocks under a hot and humid condition.
- (3) The anthracite coal samples are enriched in illite associated with kaolinite. Besides, the anthracite samples are clustered near the field of illite and are a bit offset from

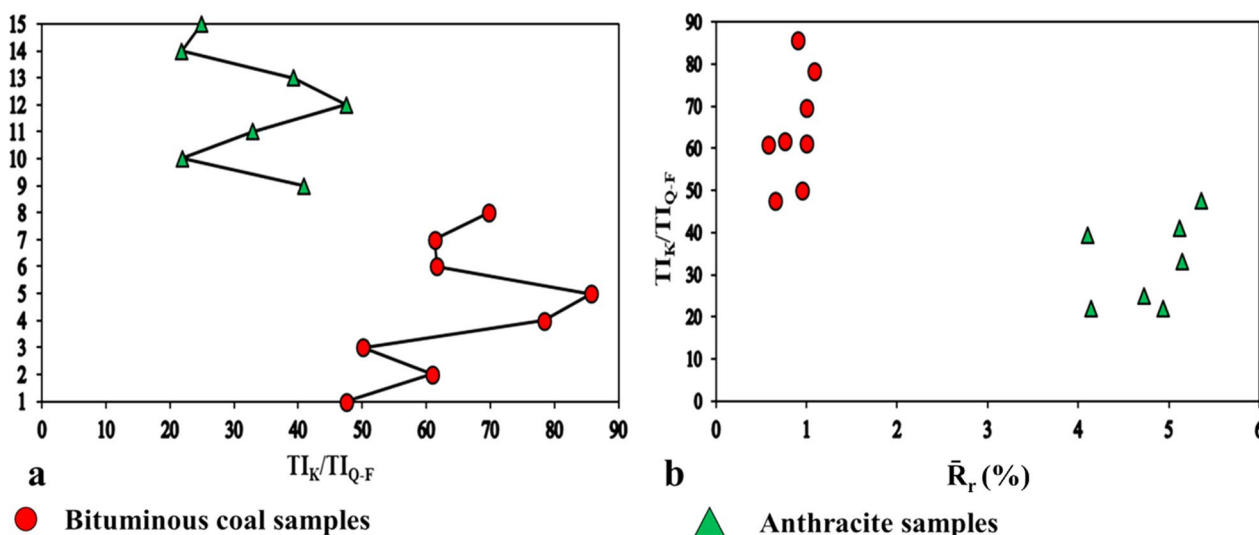


**Fig. 13** **a** Ratio of total relative intensities of kaolinite to the sum of the relative intensities of the quartz and the feldspar ( $TI_K/TI_{Q-F}$ ) showing depletion towards the anthracite samples from the bituminous samples, **b** Relation between the mean random vitrinite reflectance ( $\bar{R}_r$ ) and the total relative intensities of kaolinite to the sum of the relative intensities of the quartz and the feldspar ( $TI_K/TI_{Q-F}$ ).

*Notes:* The Y-axis in **a** represents the serial number of the samples mentioned in Table 5. 1—CG1671, 2—CG1672, 3—CG1673, 4—CG1674, 5—CG1675, 6—CG1676, 7—CG1677, 8—CG1679, 9—CG3300, 10—CG3301, 11—CG3302, 12—CG3303, 13—CG3304, 14—CG3305, 15—CG3306

**Table 7** Total relative intensities of kaolinite, quartz, and feldspar along with their ratio of the studied samples

Sample No.	$TI_K$	$TI_{Q-F}$	$TI_K/TI_{Q-F}$
CG1671	0.06	0.13	47.50
CG1672	0.34	0.57	60.86
CG1673	0.09	0.18	50.12
CG1674	0.39	0.50	78.34
CG1675	0.27	0.32	85.65
CG1676	0.42	0.69	61.61
CG1677	0.19	0.31	61.29
CG1679	0.16	0.23	69.68
CG3300	0.10	0.25	40.84
CG3301	0.03	0.14	21.91
CG3302	0.24	0.73	32.86
CG3303	0.43	0.91	47.50
CG3304	0.39	0.98	39.26
CG3305	0.26	1.19	21.85
CG3306	0.17	0.69	24.95

*Notes:*  $TI_K$  refers to total relative intensity of kaolinite,  $TI_{Q-F}$  refers to total relative intensity of quartz and feldspar,  $TI_K/TI_{Q-F}$  refers to ratio of total relative intensity of kaolinite to the total relative intensity of quartz and feldspar

the weathering trends of parent rocks in the A–CN–K diagram, which may suggest plausible influences of epigenetic potassium metasomatism that would have converted some of the kaolinite to illite.

- (4) The tectonic deformation episodes of the Himalayas brought about greenschist facies metamorphism in these anthracite samples and surrounding lithology. In this metamorphic realm, the K-metasomatism occurred as an epigenetic phenomenon altering the clay mineralogical characteristics of these anthracite samples.
- (5) The influence of the epigenetic K-metasomatism on the clay mineral framework of the anthracite samples is further confirmed from high to very high  $K_2O/Na_2O$  ratio, variations in the kaolinite/quartz content, and the declination of  $TI_K/TI_{Q-F}$  from that observed in the bituminous coal samples.
- (6) The presence of hydroxyl stretching intensity of the illite found in the FTIR spectra of the anthracite samples may further strengthen the K-metasomatic effects.

**Acknowledgements** The authors are indebted to Dr. Shimin Liu, the Learned Editor and the Learned Reviewers for their valuable feedback and suggestions to upgrade the quality of the manuscript. The authors are thankful to Mr. Amal Kishore Prasad, R&D Centre for Iron and Steel (RDCIS), Ranchi, India, for his kind co-operation in XRF analysis. They are also grateful to the Sophisticated Analytical Instrument Facility (SAIF), Indian Institute of Bombay, Mumbai, India, for the FTIR analysis.

**Authors' contributions** SG: conceptualization; writing: original draft; AO: formal analysis; data treatment; AKV: supervision; writing: review and editing.

**Funding** The authors appreciate the Department of Science and Technology (DST) India for financing the Department of Applied Geology, IIT (ISM) Dhanbad, India for acquiring modern facilities and instrument setups under the scheme of DST-FIST Level II [No- SR/FST/ES II014/2012 (C)].

**Availability of data and materials (data transparency)** The data will be made available on request.

**Code availability (software)** Not applicable.

## Declarations

**Conflict of interest** The authors declare no conflict of interest for the publication of this manuscript.

**Ethics approval (include appropriate approvals or waivers)** The authors declare that they have maintained all the ethics for the publication of this manuscript.

**Consent to participate (include appropriate statements)** Not applicable.

**Consent for publication (include appropriate statements)** The authors agree to the authorship order and provide consent for the communication and publication of this manuscript.

**Open Access** This article is licensed under a Creative Commons Attribution 4.0 International License, which permits use, sharing, adaptation, distribution and reproduction in any medium or format, as long as you give appropriate credit to the original author(s) and the source, provide a link to the Creative Commons licence, and indicate if changes were made. The images or other third party material in this article are included in the article's Creative Commons licence, unless indicated otherwise in a credit line to the material. If material is not included in the article's Creative Commons licence and your intended use is not permitted by statutory regulation or exceeds the permitted use, you will need to obtain permission directly from the copyright holder. To view a copy of this licence, visit <http://creativecommons.org/licenses/by/4.0/>.

## References

- Abart R, Badertscher N, Burkhard M, Povoden E (2002) Oxygen, carbon and strontium isotope systematics in two profiles across the Glarus thrust: implications for fluid flow. *Contrib Mineral Petrol* 143:192–208. <https://doi.org/10.1007/s00410-001-0326-5>
- Ague JJ (2003) Fluid flow in the deep crust. In: Holland HD, Turekian KK (eds) *Treatise on geochemistry*, vol 3. Elsevier, Amsterdam, pp 195–228. <https://doi.org/10.1016/B0-08-043751-6/03023-1>
- Anwita GS, Varma AK, Das SK, Pal D, Solanki G (2020) Metamorphic transformations of nitrogen functionalities: stabilization of organic nitrogen in anthracite and its effect on  $\delta^{15}\text{N}$  parameter. *Mar Pet Geol* 112:104090. <https://doi.org/10.1016/j.marpetgeo.2019.104090>
- Arndt N (2011) Greenschist facies. In: Gargaud M et al (eds) *Encyclopedia of astrobiology*. Springer, Berlin. [https://doi.org/10.1007/978-3-642-11274-4\\_675](https://doi.org/10.1007/978-3-642-11274-4_675)
- ASTM (American Society for Testing and Materials) D7582-15 (2015) Standard test methods for proximate analysis of coal and coke by macro thermogravimetric analysis, pp 1–9
- Bai Y, Liu Z, Sun P, Liu R, Hu X, Zhao H, Xu Y (2015) Rare earth and major element geochemistry of Eocene fine-grained sediments in oil shale- and coal-bearing layers of the Meihe Basin, Northeast China. *J Asian Earth Sci* 97:89–101. <https://doi.org/10.1016/j.jseaes.2014.10.008>
- Bandopadhyay AK (2010) Determination of quartz content for Indian coals using an FTIR technique. *Int J Coal Geol* 81:73–78. <https://doi.org/10.1016/j.coal.2009.10.018>
- Basu TN, Shrivastava BBP (1981) Structure and tectonics of Gondwana Basins of India. In: Cresswell MM, Vella P (eds) *International Gondwana symposium 5th* (Wellington, New Zealand), Balkema, Rotterdam, pp 172–182
- Bhattacharyya K, Mitra G (2009) A new kinematic evolutionary model for the growth of a duplex: an example from the Rangit duplex, Sikkim Himalaya, India. *Gond Res* 16:697–715. <https://doi.org/10.1016/j.gr.2009.07.006>
- Bhattacharyya K, Mitra G (2011) Strain softening along the MCT zone from the Sikkim Himalaya: relative roles of Quartz and Micas. *J Struct Geol* 33:1105–1121. <https://doi.org/10.1016/j.jsg.2011.03.008>
- Bhattacharyya K, Mitra G, Mukul M (2006) The geometry and implications of a foreland dipping duplex, the Rangit Duplex, Darjeeling–Sikkim Himalayas, India. *GSA Abstract Prog* 38:413
- Bonijoly M, Oberlin M, Oberlin A (1982) A possible mechanism for natural graphite formation. *Int J Coal Geol* 1:283–312. [https://doi.org/10.1016/0166-5162\(82\)90018-0](https://doi.org/10.1016/0166-5162(82)90018-0)
- Brooks WE (1986) Distribution of anomalously high  $\text{K}_2\text{O}$  volcanic rocks in Arizona: metasomatism at the Picacho Peak detachment fault. *Geology* 14:339–342. [https://doi.org/10.1130/0091-7613\(1986\)14%3c339:DOAHKV%3e2.0.CO;2](https://doi.org/10.1130/0091-7613(1986)14%3c339:DOAHKV%3e2.0.CO;2)
- Bullock LA, Parnell J, Perez M, Armstrong JG, Feldmann J, Boyce AJ (2018) High selenium in the Carboniferous coal measures of Northumberland, North East England. *Int J Coal Geol* 195:61–74. <https://doi.org/10.1016/j.coal.2018.05.007>
- Cao J, Wu M, Chan Y, Hu K, Bian LZ, Wang LG, Zhang Y (2012) Trace and rare earth elements geochemistry of Jurassic mudstones in the northern Qaidam basin, northwest China. *Chem Erde* 72:245–252. <https://doi.org/10.1016/j.chemer.2011.12.002>
- Chandra D (1992) Mineral resources of India 5. In: Jharia coalfield, vol 560019. Geological Society of India, Gavipuram, Bangalore, p 149
- Cox R, Lowe DR, Cullers RL (1995) The influence of sediment recycling and basement composition on evolution of mudrock chemistry in the southwestern United States. *Geochim Cosmochim Acta* 59:2919–2940. [https://doi.org/10.1016/0016-7037\(95\)00185-9](https://doi.org/10.1016/0016-7037(95)00185-9)
- Dai S, Finkelman RB (2018) Coal as a promising source of critical elements: progress and future prospects. *Int J Coal Geol* 186:155–164. <https://doi.org/10.1016/j.coal.2017.06.005>
- Dai S, Tian L, Chou C-L, Zhou Y, Zhang M, Zhao L, Wang J, Yang Z, Cao H, Ren D (2008) Mineralogical and compositional characteristics of late Permian coals from an area of high lung cancer rate in Xuanwei, Yunnan, China: occurrence and origin of quartz and chamosite. *Int J Coal Geol* 76:318–327. <https://doi.org/10.1016/j.coal.2008.09.001>
- Dai S, Guo W, Nechaev VP, French D, Ward CR, Spiro BF, Finkelman RB (2018) Modes of occurrence and origin of mineral matter in the Palaeogene coal (No. 19-2) from the Hunchun Coalfield, Jilin Province, China. *Int J Coal Geol* 189:94–110. <https://doi.org/10.1016/j.coal.2018.02.017>
- Dai S, Finkelman RB, French D, Hower JC, Graham IT, Zhao F (2021) Modes of occurrence of elements in coal: a critical evaluation. *Int J Coal Geol* 222:103815. <https://doi.org/10.1016/j.earscirev.2021.103815>

- Djomgoue P, Njopwouo D (2013) FT-IR spectroscopy applied for surface clays characterization. *JSEMAT* 3:275–282. <https://doi.org/10.4236/jsemat.2013.34037>
- Etheridge MA, Wall VJ, Cox SF, Vernon RH (1984) High fluid pressures during regional metamorphism and deformation: implications for mass transport and deformation mechanisms. *J Geophys Res Solid Earth* 89:4344–4358. <https://doi.org/10.1029/JB089iB06p04344>
- Fedo CM, Nesbitt HW, Young GM (1995) Unrevealing the effects of potassium metasomatism in sedimentary rocks and paleosols, with implications for paleoweathering conditions and provenance. *Geology* 23:921–924. [https://doi.org/10.1130/0091-7613\(1995\)023%3c0921:UTEOPM%3e2.3.CO;2](https://doi.org/10.1130/0091-7613(1995)023%3c0921:UTEOPM%3e2.3.CO;2)
- Finkelman RB (1994) Modes of occurrence of potentially hazardous elements in coal: levels of confidence. *FPT* 39:21–34. [https://doi.org/10.1016/0378-3820\(94\)90169-4](https://doi.org/10.1016/0378-3820(94)90169-4)
- Finkelman RB, Dai S, French D (2019) The importance of minerals in coal as the hosts of chemical elements: a review. *Int J Coal Geol* 212:103251. <https://doi.org/10.1016/j.coal.2019.103251>
- Fox CS (1930) The Gondwana system and related formations. *GSI Mem* 58:1–241
- French D (2018) Mineral matter in coal: friend or foe? In: Dai S, Tang Y (eds) Proceedings of 35th annual meeting of TSOP, August 17–21, 2018, Beijing, China, pp 22–23
- Gansser A (1964) *Geology of the Himalayas*. Interscience, Wiley, New York, pp 1–289
- Gee ER (1932) The geology and coal resources of Raniganj Coalfield. *GSI Mem* 61.
- Ghosh TK (1997) Petrography and metamorphism of the lower Gondwana (Permian) coal of Rangit Valley, eastern Himalays, India. *Int J Coal Geol* 33:351–368. [https://doi.org/10.1016/S0166-5162\(96\)00051-1](https://doi.org/10.1016/S0166-5162(96)00051-1)
- Ghosh SC (2002) The Raniganj Coal Basin: an example of an Indian Gondwana rift. *Sediment Geol* 147:155–176. [https://doi.org/10.1016/S0037-0738\(01\)00195-6](https://doi.org/10.1016/S0037-0738(01)00195-6)
- Ghosh S, Golding SD, Varma AK, Baublys KA (2018a) Stable isotopic composition of coal bed gas and associated formation water samples from Raniganj Basin, West Bengal, India. *Int J Coal Geol* 191:1–6. <https://doi.org/10.1016/j.coal.2018.02.019>
- Ghosh S, Rodrigues S, Varma AK, Esterle J, Patra S, Dirghangi SS (2018b) Petrographic and Raman spectroscopic of coal from Himalayan fold-thrust belts of Sikkim, India. *Int J Coal Geol* 196:246–259. <https://doi.org/10.1016/j.coal.2018.07.014>
- Ghosh S, Ojha A, Varma AK (2020) Spectral manifestations of coal metamorphism: insights from coal microstructural framework. *Int J Coal Geol* 228:103549. <https://doi.org/10.1016/j.coal.2020.103549>
- González D, Montes-Moran MA, García AB (2005) Influence of inherent coal mineral matter on the structural characteristics of graphite materials prepared from anthracites. *Energy Fuels* 19:263–269. <https://doi.org/10.1021/ef049893x>
- GSI (Geological Survey of India) (1977) Coal resources of India. *GSI Mem* 88:575
- GSI (Geological Survey of India) (2003) Coal resources of West Bengal. In: Dutt RK, Dutt AB (eds) Dutta compiled. *GSI Bull. Series A* 45:1–109.
- GSI (Geological Survey of India) (2012) Geology and mineral resources of the States of India. No. 30, Part XIX-Sikkim. ISSN 0579-4706
- Gupta S, Bickle MJ (2004) Ductile shearing, hydrous fluid channeling and highpressure metamorphism along the basement-cover contact on Sikinos, Cyclades, Greece. *Geol Soc Spec Publ* 224:161–175. <https://doi.org/10.1144/GSL.SP.2004.224.01.11>
- Gupta R, Wall TF, Baxter LA (eds) (1999) The impact of mineral impurities in solid fuel combustion. Plenum, New York, p 768
- Hayashi KI, Fujisawa H, Holland HD, Ohmoto H (1997) Geochemistry of ~ 1.9 Ga sedimentary rocks from northeastern Labrador. *Canada Geochim Cosmochim Acta* 61:4115–4137
- Hazra B, Varma AK, Bandopadhyay AK, Mendhe VA, Singh BD, Saxena VK, Samad SK, Mishra DK (2015) Petrographic insights of organic matter conversion of Raniganj basin shales, India. *Int J Coal Geol* 150–151:193–209. <https://doi.org/10.1016/j.coal.2015.09.001>
- Hazra B, Varma AK, Bandopadhyay AK, Chakravarty S, Buragohain J, Samad SK, Prasad AK (2016) FTIR, XRF, XRD and SEM characteristics of Permian shales, India. *J Nat Gas Sci Eng* 32:239–255. <https://doi.org/10.1016/j.jngse.2016.03.098>
- Hazra B, Wood DA, Varma AK, Sarkar BC, Tiwari B, Singh AK (2018a) Insights into the effects of matrix retention and inert carbon on the petroleum generation potential of Indian Gondwana shales. *Mar Pet Geol* 91:125–138. <https://doi.org/10.1016/j.marpetgeo.2017.12.028>
- Hazra B, Wood DA, Vishal V, Varma AK, Sakha D, Singh AK (2018b) Porosity controls and fractal disposition of organic-rich Permian shales using low-pressure adsorption techniques. *Fuel* 220:837–848. <https://doi.org/10.1016/j.fuel.2018.02.023>
- Hazra B, Wood DA, Kumar S, Saha S, Dutta S, Kumair P, Singh AK (2018c) Fractal disposition, porosity characterization and relationships to thermal maturity for the Lower Permian Raniganj basin shales, India. *J Nat Gas Sci Eng* 59:452–465. <https://doi.org/10.1016/j.jngse.2018.09.014>
- Hu W, Hou W, Dong H, Chen H, Xia Q, Sun Y (2021) Enhancement of biogenic methane production from subbituminous coal by reduced iron-bearing clay mineral. *Int J Coal Geol* 248:103862. <https://doi.org/10.1016/j.coal.2021.103862>
- Huang X, Gordon T, Rom WN, Finkelman RB (2006) Interaction of iron and calcium minerals in coals and their roles in coal dust-induced health and environmental problems. *Rev Mineral Geochem* 64:153–178. <https://doi.org/10.2138/rmg.2006.64.6>
- ISO (International Organization for Standardization) (2005) Classification of coals. ISO 11760:2005(E), 1st edn. ISO, Geneva
- ISO 14180 (International Organization for Standardization) (2017) Solid mineral fuels—guidance on the sampling of coal seams. ISO, Geneva
- ISO 18283 (International Organization for Standardization) (2006) Hard coal and coke—manual sampling. ISO, Geneva
- Kang HP, Lin J, Fan MJ (2015) Investigation on support pattern of a coal mine roadway within soft rocks—a case study. *Int J Coal Geol* 140:31–40. <https://doi.org/10.1016/j.coal.2015.01.003>
- Large D, Kelly S, Spiro B, Tian L, Shao L, Finkelman RB, Zhang M, Somerfield C, Plint S, Ali Y, Zhou Y (2009) Silica–volatile interaction and the geological cause of the Xuan Wei lung cancer epidemic. *Environ Sci Technol* 43:9016–9021. <https://doi.org/10.1021/es902033j>
- Larsen J, Hu J (2006) Kerogen Chemistry 8. Hydrous pyrolysis of rundle kerogen: source of the oxygen in CO<sub>2</sub> and mineral catalysis. *Energy Fuels* 20:278–280. <https://doi.org/10.1021/ef050237m>
- Li Q, Shi W, Yang R (2016) Deformation mechanisms in a coal mine roadway in extremely swelling soft rock. *Springerplus* 5(1):1310. <https://doi.org/10.1186/s40064-016-2942-6>
- Lin R, Soong Y, Granite EJ (2018) Evaluation of trace elements in U.S. coals using the USGS COALQUAL database version 3.0. Part II: non-REY critical elements. *Int J Coal Geol* 192:39–50. <https://doi.org/10.1016/j.coal.2018.04.005>
- Liu S, Ma W, French D, Tuo K, Mei X (2019) Sequential mineral transformation during underground coal gasification with the presence of coal partings. *Int J Coal Geol* 208:1–11. <https://doi.org/10.1016/j.coal.2019.04.003>
- Ma X, Zheng J, Zheng G, Xu W, Qian Y, Xia Y, Wang Z, Wang X, Ye X (2016) Influence of pyrite on hydrocarbon generation during



- pyrolysis of type-III kerogen. *Fuel* 167:329–336. <https://doi.org/10.1016/j.fuel.2015.11.069>
- Manning CE, Ingebritsen SE (1999) Permeability of the continental crust: implications of geothermal data and metamorphic systems. *Rev Geophys* 37:127–150. <https://doi.org/10.1029/1998RG90002>
- Mark C, Molinda GM (2005) The Coal Mine Roof Rating (CMRR)—a decade of experience. *Int J Coal Geol* 64:85–103. <https://doi.org/10.1016/j.coal.2005.03.007>
- Marsh H, Warburton AP (1970) Catalysis of graphitization. *J Appl Chem* 20:133–142. <https://doi.org/10.1002/jctb.5010200409>
- McCaig AM, Wayne DM, Marshall JD, Banks D, Henderson I (1995) Isotopic and fluid inclusion studies of fluid movement along the Gavarnie Thrust, central Pyrenees; reaction fronts in carbonate mylonites. *Am J Sci* 295:309–343. <https://doi.org/10.2475/ajs.295.3.309>
- McLennan SM, Hemming S, McDaniel DK, Hanson GN (1993) Geochemical approaches to sedimentation, provenance, and tectonics. *Geol Soc Am Spec Pap* 284:21–40. <https://doi.org/10.1130/SPE284-p21>
- Mishra HK, Cook AC (1992) Petrology and thermal maturity of coals in the Jharia Basin: implications for oil and gas origins. *Int J Coal Geol* 20:277–313. [https://doi.org/10.1016/0166-5162\(92\)90018-R](https://doi.org/10.1016/0166-5162(92)90018-R)
- Misra S, Varma AK, Das SK, Mani D, Biswas S (2018) Thermal controls of lamprophyre sill on hydrocarbon generation outlook of shale beds in Raniganj Basin, India. *J Nat Gas Sci Eng* 56:536–548. <https://doi.org/10.1016/j.jngse.2018.06.028>
- Misra S, Varma AK, Hazra B, Biswas S, Samad SK (2019) The influence of the thermal aureole asymmetry on hydrocarbon generative potential of coal beds: insights from Raniganj Basin, West Bengal, India. *Int J Coal Geol* 206:91–105. <https://doi.org/10.1016/j.coal.2019.03.008>
- Moradi AV, Sarı A, Akkaya P (2016) Geochemistry of the Miocene oil shale (Hançili Formation) in the Çankırı–Çorum Basin, Central Turkey: implications for Paleoclimate conditions, source–area weathering, provenance and tectonic setting. *Sediment Geol* 341:289–303. <https://doi.org/10.1016/j.sedgeo.2016.05.002>
- Mukhopadhyay G, Mukhopadhyay SK, Roychowdhury M, Parui PK (2010) Stratigraphic correlation between different Gondwana basins of India. *J Geol Soc India* 76:251–266. <https://doi.org/10.1007/s12594-010-0097-6>
- Nesbitt HW, Young GM (1982) Early Proterozoic climates and plate motions inferred from major element chemistry of lutites. *Nature* 199:715–717. <https://doi.org/10.1038/299715a0>
- Oberlin A, Terriere G (1975) Graphitization studies of anthracites by high resolution electron microscopy. *Carbon* 13:367–376. [https://doi.org/10.1016/0008-6223\(75\)90004-4](https://doi.org/10.1016/0008-6223(75)90004-4)
- Oliver NHS (1996) Review and classification of structural controls on fluid flow during regional metamorphism. *J Metamorph Geol* 14:477–492. <https://doi.org/10.1046/j.1525-1314.1996.00347.x>
- Oya A, Marsh H (1982) Review phenomena of catalytic graphitization. *J Mater Sci* 17(2):309–322. <https://doi.org/10.1007/BF00591464>
- Painter PC, Snyder RW, Starsinic M, Coleman MM, Kuehn DW, Davis A (1981) Concerning the application of FT-IR to the study of coal; a critical assessment of band assignments and the application of spectral analysis programs. *Appl Spectrosc* 35(5):475–485. <https://doi.org/10.1366/0003702814732256>
- Pitcairn IK, Skelton ADL, Broman C, Arghe F, Boyce A (2010) Structurally focused fluid flow during orogenesis: the Islay Anticline, SW Highlands, Scotland. *J Geol Soc London* 167:659–674. <https://doi.org/10.1144/0016-76492009-135>
- Putnis A, Austrheim H (2010) Fluid-induced processes: metasomatism and metamorphism. *Geofluids* 10:254–269. <https://doi.org/10.1111/J.1468-8123.2010.00285.X>
- Raask E (1985) The mode of occurrence and concentration of trace elements in coal. *Prog Energy Combust* 11:97–118. [https://doi.org/10.1016/0360-1285\(85\)90001-2](https://doi.org/10.1016/0360-1285(85)90001-2)
- Ray SK (1995) Lateral variations in geometry of thrust planes and its significance, as studied in the Shumar allochthon, Lesser Himalayas, eastern Bhutan. *Tectonophysics* 249:125–139. [https://doi.org/10.1016/0040-1951\(95\)00008-B](https://doi.org/10.1016/0040-1951(95)00008-B)
- Rodrigues S, Suárez-Ruiz I, Marques M, Flores D (2012) Catalytic role of mineral matter in structural transformation of anthracites during high temperature treatment. *Int J Coal Geol* 93:49–55. <https://doi.org/10.1016/j.coal.2012.01.012>
- Roser BP, Korsch RJ (1986) Determination of tectonic setting of sandstone mudstone suites using SiO<sub>2</sub> content and K<sub>2</sub>O/Na<sub>2</sub>O ratio. *J Geol* 94:635–650. [www.jstor.org/stable/30078330](http://www.jstor.org/stable/30078330)
- Saikia BJ, Parthasarathi G (2010) Fourier transform infrared spectroscopic characterization of kaolinite from Assam and Meghalaya, Northeastern India. *J Mod Phys* 1:206–210. <https://doi.org/10.4236/jmp.2010.14031>
- Schwan W (1980) In: Saklani PS (ed) Shortening structures in eastern and northwestern Himalayan rocks. Today and Tomorrow's Printers and Publishers, New Delhi
- Selverstone J, Franz G, Thomas S, Getty S (1992) Fluid variability in 2 GPa eclogites as an indicator of fluid behavior during subduction. *Contrib Mineral Petrol* 112:341–357. <https://doi.org/10.1007/BF00310465>
- Sengupta N (1980) A revision of the Geology of the Jharia Coalfield with particular reference to distribution of coal seams. Ph.D. thesis, Indian School of Mines, Dhanbad
- Seredin VV, Finkelman RB (2008) Metalliferous coals: a review of the main genetic and geochemical types. *Int J Coal Geol* 76:253–289. <https://doi.org/10.1016/j.coal.2008.07.016>
- Singh DP, Hazra B, Wood DA, Singh PK (2021) Hydrocarbon generation and kinetics: a case study of Permian shales. *India J Asian Earth Sci* 222:104960. <https://doi.org/10.1016/j.jseaes.2021.104960>
- Skelton ADL, Graham CM, Bickle MJ (1995) Lithological and structural controls on regional 3-D fluid flow patterns during greenschist facies metamorphism of the Dalradian of the SW Scottish Highlands. *J Petrol* 36:563–586. <https://doi.org/10.1093/petrology/36.2.563>
- Solomon PR, Carangelo RM (1982) FTIR analysis of coal. 1. Techniques and determination of hydroxyl concentrations. *Fuel* 61:663–669. [https://doi.org/10.1016/0016-2361\(82\)90014-X](https://doi.org/10.1016/0016-2361(82)90014-X)
- Tao S, Xu Y, Tang D, Xu H, Li S, Chen S, Liu W, Cui Y, Gou M (2017) Geochemistry of the Shitoumei oil shale in the Santanghu Basin, Northwest China: implications for paleoclimate conditions, weathering, provenance and tectonic setting. *Int J Coal Geol* 184:42–56. <https://doi.org/10.1016/j.coal.2017.11.007>
- Tian L (2005) Coal combustion emissions and lung cancer in Xuan Wei, China. Ph.D. thesis. University of California, Berkeley
- Tian L, Dai S, Wang J, Huang Y, Ho SC, Zhou Y, Lucas D, Koshland CP (2008) Nanoquartz in late Permian C1 coal and the high incidence of female lung cancer in the Pearl River Origin area: a retrospective cohort study. *BMC Public Health* 8:398. <https://doi.org/10.1186/1471-2458-8-398>
- Tiwari B, Ojha A, Ghosh S, Varma AK, Mendhe VA, Mondal A (2020) A composite microstructural and geochemical approach to quench the quest for hydrocarbon from Barren measures shales of Jharia Basin. *India J Nat Gas Sci Eng* 78:103310. <https://doi.org/10.1016/j.jngse.2020.103310>
- Valdiya KS (1980) Geology of the Kumaun Lesser Himalaya. The Himachal Press, Wadia Institute of Himalayan Geology, Dehra Dun, pp 1–219
- Varma AK, Hazra B, Samad SK, Panda S, Mendhe VA (2014) Methane sorption dynamics and hydrocarbon generation of shale samples

- from West Bokaro and Raniganj basins, India. *J Nat Gas Sci Eng* 21:1138–1147. <https://doi.org/10.1016/j.jngse.2014.11.011>
- Varma AK, Mishra DK, Samad SK, Prasad AK, Panigrahi DC, Mendhe VA, Singh BD (2018) Geochemical and organo-petrographic characterization for hydrocarbon generation from Barakar Formation in Auranga Basin, India. *Int J Coal Geol* 186:97–114. <https://doi.org/10.1016/j.coal.2017.12.002>
- Verma RP (1983) Exploration strategy for preparing master plan for reconstruction and development of a complex coalfield in India. In: Austin R (ed) *International coal exploration symposium*, 4th. Miller Freeman, Sydney, pp 1–23
- Wang J, Morishita K, Takarada T (2001) High-temperature interactions between coal char and mixtures of calcium oxide, quartz and kaolinite. *Energy Fuels* 15:1145–1152. <https://doi.org/10.1021/ef0100092>
- Wang L, Qiu T, Guo Z, Shen X, Yang J, Wang Y (2021) Changes and migration of coal-derived minerals on the graphitization process of anthracite. *ACS Omega* 6:180–187. <https://doi.org/10.1021/acsomega.0c04120>
- Ward CR (ed) (1984) *Coal geology and coal technology*. Blackwell, Melbourne, p 345
- Ward CR (2002) Analysis and significance of mineral matter in coal seams. *Int J Coal Geol* 50:135–168. [https://doi.org/10.1016/S0166-5162\(02\)00117-9](https://doi.org/10.1016/S0166-5162(02)00117-9)
- Ward CR (2016) Analysis, origin and significance of mineral matter in coal: an updated review. *Int J Coal Geol* 165:1–27. <https://doi.org/10.1016/j.coal.2016.07.014>
- Worash G (2002) Geochemistry provenance and tectonic setting of the Adigrat sandstone northern Ethiopia. *J Afr Earth Sci* 35:185–198. [https://doi.org/10.1016/S0899-5362\(02\)00126-4](https://doi.org/10.1016/S0899-5362(02)00126-4)
- Yang N, Hu G, Qin W, Huang J (2021) Experimental study on mineral variation in coal under microwave irradiation and its influence on coal microstructure. *J Nat Sci Eng* 96:104303. <https://doi.org/10.1016/j.jngse.2021.104303>
- Yardley BWD, Gleeson S, Bruce S, Banks D (2000) Origin of retrograde fluids in metamorphic rocks. *J Geochem Explor* 69:281–285. [https://doi.org/10.1016/S0375-6742\(00\)00132-1](https://doi.org/10.1016/S0375-6742(00)00132-1)
- Zhang K, Jin W, Lin H, Dong C, Wu S (2018) Major and trace elemental compositions of the upper Carboniferous Batamayneishan mudrocks, Wulungu area, Junggar Basin, China: implications for controls on the formation of the organic-rich source rocks. *Mar Pet Geol* 91:550–561. <https://doi.org/10.1016/j.marpetgeo.2018.01.003>
- Zhao ZY, Zhao JH, Wang HJ, Liao JD, Liu CM (2007) Distribution characteristics and applications of trace elements in Junggar Basin. *Nat Gas Explor Dev* 30:30–33 (in Chinese with English abstract)
- Zhao L, Ward CR, French D, Graham IT (2013) Mineralogical composition of Late Permian coal seams in the Songzao Coalfield, southwestern China. *Int J Coal Geol* 116–117:208–226. <https://doi.org/10.1016/j.coal.2013.01.008>
- Zhao L, Ward CR, French D, Graham IT, Dai S, Yang C, Xie P, Zhang S (2018) Origin of a kaolinite-NH<sub>4</sub>-illite-pyrophyllite-chlorite assemblage in a marine-influenced anthracite and associated strata from the Jincheng Coalfield, Qinshui Basin, Northern China. *Int J Coal Geol* 185:61–78. <https://doi.org/10.1016/j.coal.2017.11.013>

**Publisher's Note** Springer Nature remains neutral with regard to jurisdictional claims in published maps and institutional affiliations.